



Influence of ridge migration and proximity to hot spots on the morphology of slow- and intermediate-spreading centers

S. Supak

*Department of Earth Science, University of California at Santa Barbara, Santa Barbara, California 93106, USA
(supak@ldeo.columbia.edu)*

Lamont-Doherty Earth Observatory of Columbia University, Palisades, New York 10964, USA

S. M. Carbotte

Lamont-Doherty Earth Observatory of Columbia University, Palisades, New York 10964, USA

K. C. Macdonald

Department of Earth Science, University of California at Santa Barbara, Santa Barbara, California 93106, USA

[1] Recent observations of ridge bathymetry suggest magmatic segmentation at fast- and intermediate-spreading centers is linked to the migration of the spreading axis over the mantle. At fast- and intermediate-spreading centers, Carbotte et al. (2004) observed that leading segments, those that are offset in the direction of ridge migration, are typically shallower (interpreted to be magmatically robust) relative to trailing segments across first- and second-order discontinuities. The model set forth for this correlation invokes asymmetrical mantle upwelling in response to the absolute motion of the ridge axis and the entrainment of melt from across discontinuities. In this investigation, differences in ridge axis depth across first- and second-order discontinuities are examined within the context of absolute plate motions for portions of the slow-spreading Mid-Atlantic Ridge (MAR 22–36°N and 25–35°S latitude), intermediate-spreading Galápagos Spreading Center (GSC 83–98°W), and intermediate-spreading South East Indian Ridge (SEIR 77–114°E). Portions of each of these areas display chemical and/or physical anomalies resulting from hot spot–ridge interaction. Along non–hot spot–influenced sections of intermediate-spreading ridges, leading segments coincide with shallower segments across 72% of the first- and second-order discontinuities (86% of transform faults and 55% of second-order discontinuities). Depth asymmetries vary with ridge offset length, with maximum asymmetries for ridge offset lengths of 50–100 km. A weaker correlation is observed between ridge migration direction and ridge morphology at the slow-spreading MAR, where leading segments are shallower across ~60% of first- and second-order discontinuities. For hot spot–influenced spreading centers, hot spot proximity dominates ridge morphology at intermediate-spreading centers, but it is not a consistent predictor of axial depth asymmetries at slow-spreading centers. This spreading-rate-dependent influence of ridge migration and hot spot proximity on axial morphology may reflect a more limited entrainment of melt from across slow-spreading discontinuities due to the predominance of three-dimensional upwelling and melt focusing to segment centers.

Components: 11,308 words, 12 figures, 2 tables.

Keywords: ridge morphology; hot spots; ridge migration; magma supply.

Index Terms: 3035 Marine Geology and Geophysics: Midocean ridge processes; 3037 Marine Geology and Geophysics: Oceanic hotspots and intraplate volcanism; 3040 Marine Geology and Geophysics: Plate tectonics (8150, 8155, 8157, 8158); 3045 Marine Geology and Geophysics: Seafloor morphology, geology, and geophysics.

Received 9 June 2006; **Revised** 25 August 2006; **Accepted** 25 September 2006; **Published** 31 January 2007.

Supak, S., S. M. Carbotte, and K. C. Macdonald (2007), Influence of ridge migration and proximity to hot spots on the morphology of slow- and intermediate-spreading centers, *Geochem. Geophys. Geosyst.*, 8, Q01010, doi:10.1029/2006GC001387.

1. Introduction

[2] Morphological segmentation is a fundamental characteristic of mid-ocean ridges (MORs) with systematic changes in the depth and width of the ridge axis observed at all spreading rates [e.g., Macdonald *et al.*, 1988; Lin *et al.*, 1990]. Typically, the ridge axis deepens toward transform faults and smaller offset discontinuities, leading to an undulating axial depth profile. However, changes also are observed between segments where one segment is shallower than the adjacent segment across a ridge offset. This topographic variability is commonly attributed to differences in magma flux from the mantle, with shallower regions along the MOR interpreted as locations of greater magma supply [e.g., Lin *et al.*, 1990; Scheirer and Macdonald, 1993; Thibaud *et al.*, 1998]. Although it is widely accepted that variations in ridge morphology reflect an underlying magmatic segmentation, the origin of this segmentation and its significance for melting and flow in the mantle are subjects of ongoing debate.

[3] Independent of spreading rate, a MOR migrates with respect to the deeper mantle at a rate and direction determined by the absolute motions of the bounding plates [Stein *et al.*, 1977]. Therefore MORs are not “fixed” above the mantle in the hot spot reference frame, but rather they can be envisioned as sampling mantle as they migrate over it. Recent observations of ridge bathymetry [Carbotte *et al.*, 2004] suggest that magmatic segmentation at fast- (>80 mm/yr full-rate) and intermediate-spreading (50–80 mm/yr) centers is linked to the migration of the spreading axis over the mantle. Comparisons of ridge-axis depths across transform faults and nontransform discontinuities show that segments offset in the direction of ridge migration (leading, Figure 1) are consistently shallower than adjacent trailing segments. Carbotte

et al. [2004] propose that this correlation between ridge morphology and plate kinematics results from an asymmetry in mantle upwelling triggered by ridge migration over the mantle [e.g., Davis and Karsten, 1986; Schouten *et al.*, 1987; Wilson, 1992], coupled with melt entrainment to ridge segments across discontinuities (Figure 2). Assuming temperature- and pressure-dependent viscosity, Katz *et al.* [2004] present 2-D numerical simulations that confirm asymmetric melt production is expected beneath migrating spreading centers and results from the motion of the lithospheric notch, associated with plate spreading, over the asthenosphere.

[4] Faster upwelling and greater melt production beneath an advancing plate alone would not result in asymmetry in melt delivery to adjacent ridge segments. However, melt delivery from the mantle is believed to involve focusing of melts from a broad upwelling zone beneath the spreading center; and, any location along the ridge axis is presumably fed by melts generated from a broad volume within the mantle [e.g., Sparks and Parmentier, 1993; Magde and Sparks, 1997; Forsyth *et al.*, 1998]. Carbotte *et al.* [2004] suggest that near segment ends melt focusing may lead to entrainment of melts across discontinuities from the upwelling zone of adjacent ridge segments, with leading segments tapping melt from the faster-upwelling and hence more melt-rich zone beneath an advancing plate (Figure 2). While both segment ends are expected to be locations of reduced melt delivery relative to elsewhere along the ridge (Figure 2b), the differences in melt production beneath advancing and trailing plates leads to a local asymmetry in melt availability across discontinuities. This “melt entrainment” effect may be restricted to segment ends unless significant redistribution of melt occurs within segments at shallow mantle and/or crustal levels.

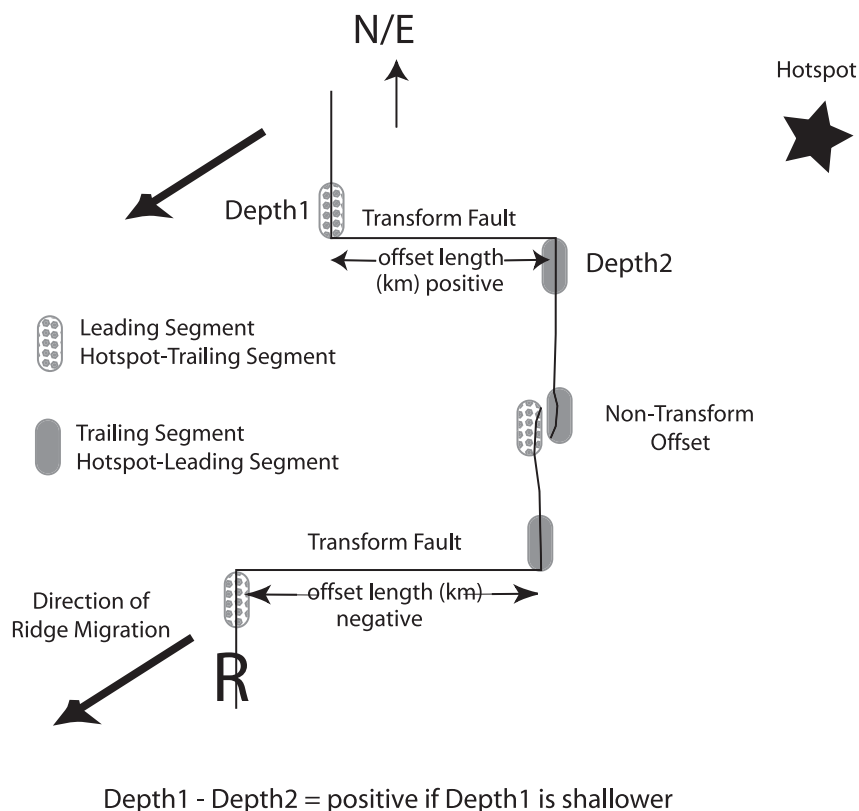


Figure 1. Illustration of ridge segment geometry and terminology used in this study. MOR segments offset in the direction of ridge migration at ridge axis discontinuities are termed leading segments, and those segments with an opposite sense of offset are termed trailing segments. Segments offset toward a hot spot, relative to adjacent segments, are referred to as hot spot–leading segments. For all four of the MOR regions examined in this study, the ridge axis migrates away from the hot spot and hence all leading segments are also hot spot–trailing. Sign convention adopted for measurements of discontinuity offset length and axial depth differences are relative to a viewer on the ridge at R facing north for the MAR and east for GSC and SEIR as shown (see Tables 1 and 2).

[5] The study of *Carbotte et al.* [2004] focused on portions of fast- and intermediate-spreading MORs; however, differences in segment morphology are observed at all spreading rates. Slow-spreading centers (<50 mm/yr) have a distinctly different morphology and magma plumbing system than fast- and intermediate-spreading centers, with strong gradients in a range of ridge properties within individual segments. Unlike the East Pacific Rise (~80–150 mm/yr full-rate) where a nearly continuous magma body is imaged beneath much of the axial zone [*Detrick et al.*, 1987, 1993], the Mid-Atlantic Ridge (MAR ~ 20–40 mm/yr full-rate) appears to lack a steady state magma chamber within much of the crust. Instead, the inner valley floor is speckled with axial volcanoes, which are believed to be fed by discrete magma pockets [e.g., *Smith and Cann*, 1993]. It is generally accepted that the shallow mid-segment regions of slow-spreading ridges are places of focused melt supply

to the crust [*Lin et al.*, 1990; *Crawford et al.*, 2005]. Both seismic and gravity data indicate thicker crust at segment centers compared with segment ends [e.g., *Lin et al.*, 1990; *Tolstoy et al.*, 1993; *Dunn et al.*, 2005]; and, what evidence exists for higher crustal temperatures and/or melt at the MAR is found only at segment centers. For example, *Magde et al.* [2000] imaged a ~10-km-diameter low-velocity anomaly (–0.4 km/s) within a segment center on the MAR at ~35°N; and, *Singh et al.* [2005] recently showed evidence for an axial magma chamber beneath the central volcano within the Lucky Strike Segment of the MAR, near ~37°N.

[6] In addition to spreading rate, proximity to hot spots is known to exert a strong influence on ridge morphology. Hot spot–ridge interaction affects up to 20% of the world’s MOR system with long-wavelength gradients observed in chemical and physical properties, extending up to 1000s of kilo-

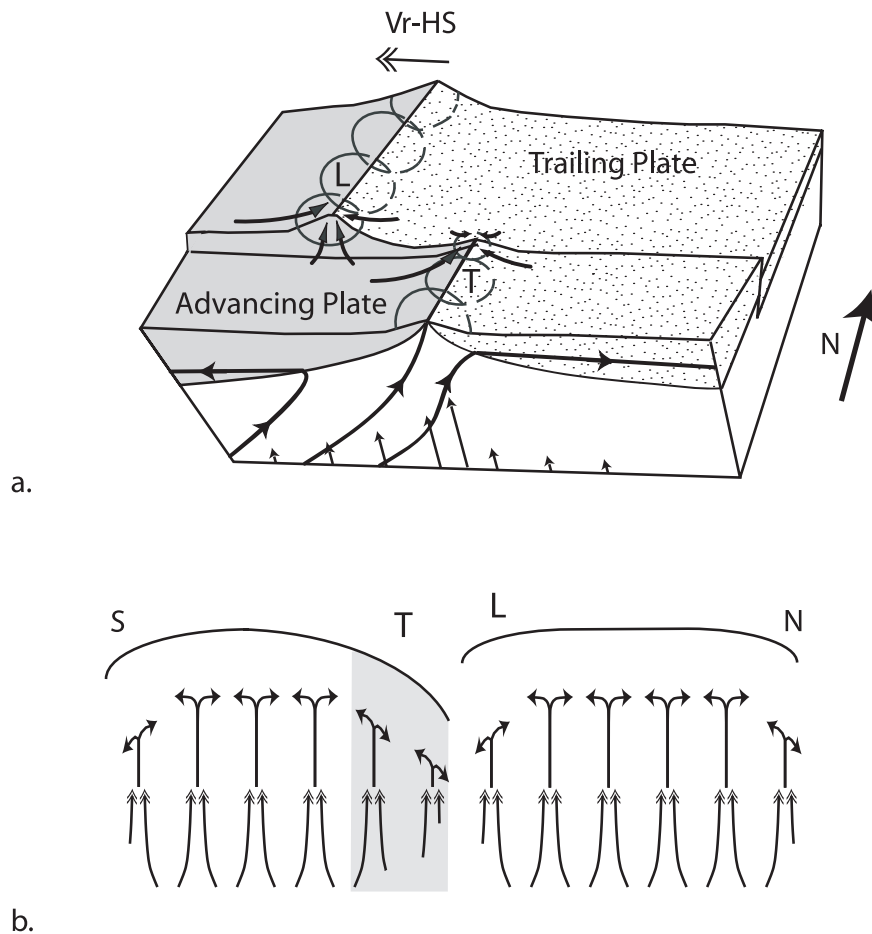


Figure 2. Schematics illustrating the “melt entrainment” model. (a) For a migrating MOR, asymmetry exists in the mantle flow paths beneath both an advancing (gray shaded) and trailing plate, with more rapid mantle upwelling and greater melt production predicted beneath the advancing plate (vertical arrows). The circles along the ridge axis encompass idealized regions of mantle melt focusing, with circle size proportional to relative melt volumes entrained to the ridge axis. Near the ends of ridge segments, melt volumes are limited by the presence of a nearby discontinuity. However, if melts are entrained across a discontinuity from the upwelling zone of the neighboring segment, asymmetry in melt availability is expected (arrows show possible melt migration paths). Whereas leading segments (L) tap melt from the more rapidly upwelling melt rich zone of an advancing plate, trailing segments (T) draw melt from the less rapidly upwelling trailing plate. Streamlines (thick lines) indicate the motion of asthenosphere relative to a stationary observer on the ridge axis. Modified from *Carbotte et al.* [2004]. (b) Along-axis profile view of melt delivery corresponding to the migrating MOR shown in Figure 2a. Double-headed arrows represent focusing of mantle melts beneath the ridge axis from a broad mantle melt source region. These melts may be redistributed along-axis at shallow mantle and/or crustal levels (single-headed arrows). Total mantle melt flux is reduced near ridge segment ends with melts drawn, in part, from the distal ends of the upwelling zone of the adjacent segment. However, for the case of a migrating MOR, leading segments tap melts from the more melt rich advancing plate side of the neighboring segment’s mantle upwelling zone (Figure 2a). Idealized region of less melt availability at a trailing segment is shown in gray.

meters along the ridge from the hot spot source [*Ito et al.*, 2003]. Portions of the MOR influenced by a nearby hot spot typically are associated with shallower depths, thicker crust as determined from seismic studies and gravity anomalies, and ridge-axis basalts with enriched geochemistry [e.g., *Ito et al.*, 1999; *Canales et al.*, 2002; *Darbyshire et al.*, 2000; *Schilling et al.*, 1983].

[7] In this investigation, inter-segment elevation differences across first- and second-order discontinuities along the slow-spreading Mid-Atlantic Ridge (NMAR 22–36°N and SMAR 25–35°S), intermediate-rate Galápagos Spreading Center (GSC 83–98°W) and South East Indian Ridge (SEIR 77–114°E) are examined within the context of absolute plate motions. One objective of the

study is to examine the relationship between MOR migration and ridge morphology for the slow-to-intermediate range of spreading rates. Another objective is to examine the relationship between the morphological segmentation of a MOR, ridge migration and proximity to a hot spot. At slow-spreading ridges, we find little correlation between ridge depths across discontinuities and both ridge migration direction and hot spot proximity, whereas a much stronger correlation is found at intermediate- and fast-spreading rates [Carbotte *et al.*, 2004; this study]. This spreading-rate dependence is interpreted as reflecting different patterns of mantle upwelling and melt delivery from the mantle.

2. Methods

[8] In this study we use shipboard multibeam bathymetric data publicly available through the Ridge Multibeam Synthesis Project (<http://www.marine-geo.org>). We focus only on regions of the global MOR where continuous data coverage of the axial region is available. The data are compiled from studies of Kong *et al.* [1989], Purdy *et al.* [1990], Sempéré *et al.* [1990], Sloan and Patriat [1992], Gente *et al.* [1995], Magde *et al.* [1997], Tucholke *et al.* [1997], and Smith *et al.* [2002] for the NMAR, Fox *et al.* [1991], Grindlay *et al.* [1991], and Weiland *et al.* [1996] for the SMAR, Hey *et al.* [1986], Phipps Morgan *et al.* [1988], Perram and Macdonald [1994], Carbotte and Macdonald [1994], Mutter [1995], Canales *et al.* [1997], Sinton *et al.* [2003], and Christie *et al.* [2005] for the GSC, and Cochran *et al.* [1997], Sempéré *et al.* [1997], and Scheirer *et al.* [1998] for the SEIR.

[9] Digitized ridge axis locations were obtained for the SEIR from Cochran *et al.* [1997] for $\sim 100.3^\circ\text{E}$ to $\sim 114^\circ\text{E}$ and $\sim 88.7^\circ$ to $\sim 91.9^\circ\text{E}$ and from Scheirer *et al.* [1998] for the region west of $\sim 88.1^\circ\text{E}$. For all other regions, the integrated mapping and visualization tool, GeoMapApp (<http://www.marine-geo.org/geomapapp/>) was used to identify and digitize the ridge axis. GeoMapApp provides access to a gridded global bathymetry compilation of publicly available data as well as tools for extracting bathymetric profiles and digitizing locations [Haxby *et al.*, 2003]. The axis was identified by following the crest of axial volcanic ridges and other volcanic constructs within the axial rift valley floor or by following the approximate midpoint between the innermost pair of axis-facing faults. The bathymetric profile tool in GeoMapApp enables cross-axis profiles to be

drawn instantaneously, which greatly aided our axis identification. Where the original data source publications listed above included figures of ridge axis bathymetry and interpreted axis locations in sufficient resolution, these were used to guide our interpretation. An example of our axis identification for a portion of the SMAR is shown in Figure 3a.

[10] For each study area, all first- and second-order discontinuities were identified and numbered. We define first-order discontinuities as transform faults with a well defined ridge-perpendicular bathymetric depression and offset length greater than 20 km. Second-order discontinuities at slow-spreading centers are typified by a bend or jog in the rift valley [Macdonald, 1986; Macdonald *et al.*, 1988; Grindlay *et al.*, 1991]. In this study, we group discontinuities that offset the ridge axis by 5 to 25 km and for which no ridge-perpendicular fracture trace is evident as second-order discontinuities. The one exception to this definition is discontinuity N17, which is an oblique trending offset of ~ 60 km composed of two short en echelon rift valley segments that are grouped here as a second-order discontinuity.

[11] Digitized ridge axis locations for each ridge segment were interpolated at evenly spaced intervals of 250 m (Figure 3b). Seafloor depths were sampled at each interpolated location from bathymetry grids (100 m grid node spacing) using a nearest neighbor interpolation algorithm available in MATLAB (command LTLN2VAL). To remove the effects of small-scale topographic anomalies associated with, for example, small volcanic cones and mounds, moving averages were calculated for along axis seafloor depth using box filters 1 km wide along-axis and of varying cross-axis width (0.4, 1.0 and 2.0 km) (Figure 3c). This range of box filters was chosen to assess the influence of cross-axis volcanic topography on along-axis depth variations. In all regions we find similar wavelength along-axis relief irrespective of filter width, although in places, the amplitude of relief differs significantly with averaging area. For example, seafloor depths calculated for the 2 km wide box filter are systematically greater in regions where axial volcanic ridges within the rift valley floor of the MAR are narrower than this maximum filter size (e.g., Figure 3). Average differences between depths obtained with the narrowest (0.4 km) and wider (1 km/2 km) box filters range from 11 m/24 m for the GSC up to 27 m/47 m for the NMAR. All results presented in this paper use the narrowest

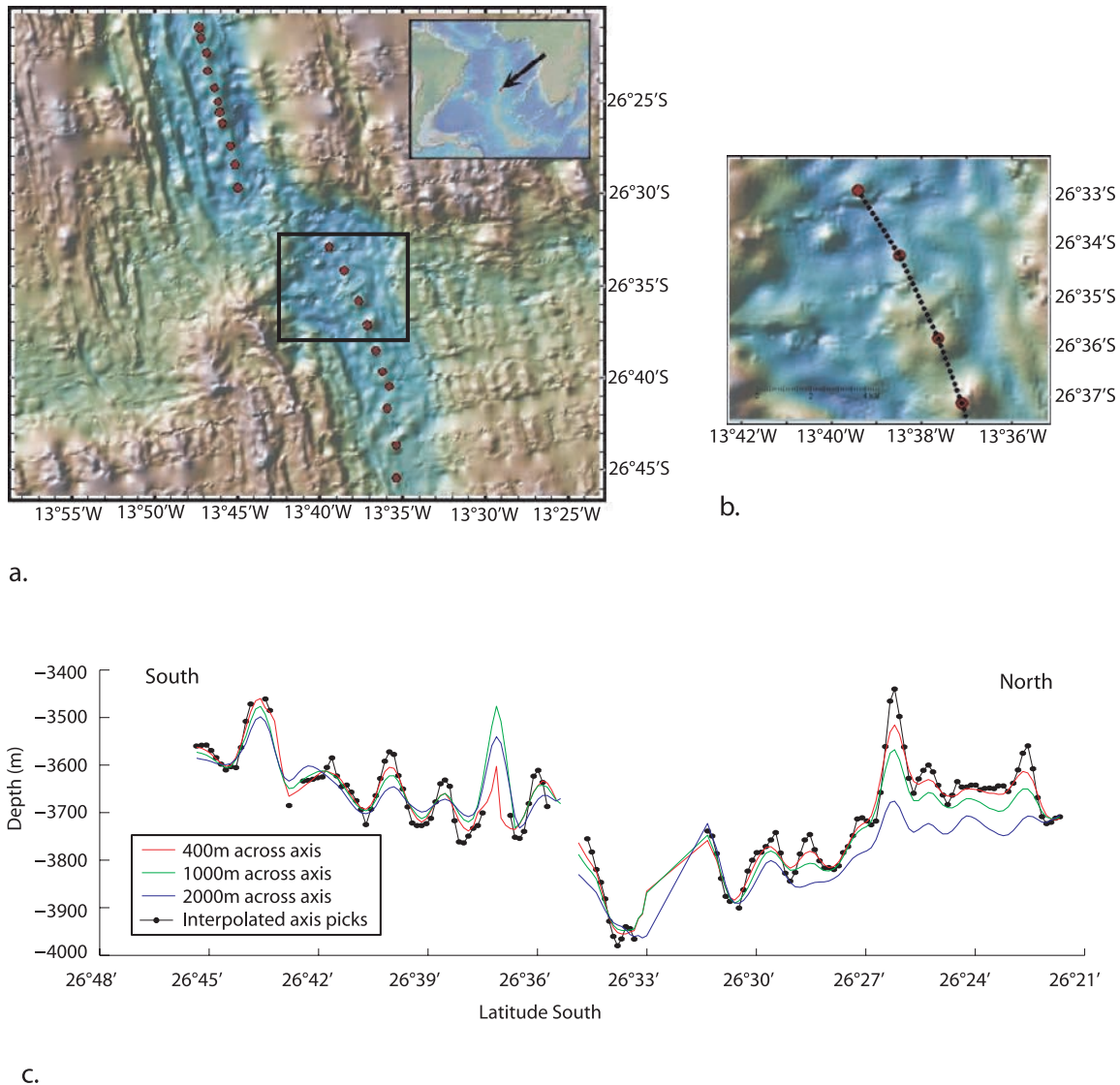


Figure 3. Example of axis picks from the SMAR. (a) Original axis picks obtained using digitizer option in GeoMapApp shown in red. (b) Black dots represent the interpolated axis. (c) Interpolated axial depth profile in black, along with three box filtered profiles (1 km wide along axis and of varying cross-axis width). All results presented in this paper use the smallest spatial filter width of 400 m across-axis.

spatial filter width of 400 m across-axis. We assume this width coincides with the neovolcanic zone along axial high segments and the crest of axial volcanic ridges where present within rift valley segments.

[12] For each ridge segment, the smoothed ridge-axis depth profile was used to determine average depth for the segment, depth at the shallowest point, and depths at 5, 10 and 15 km from both ends of the segment. Average segment depths and segment shallowest point depths are shown on bathymetric maps for each area (Figures 4a, 5a, 6a, and 7a). Whereas a leading and trailing seg-

ment end can be defined for each discontinuity, an entire segment can be classified as leading or trailing only if the bounding discontinuities step in opposite directions (Figure 1). As only a subset of the ridge axis has this geometry, we focus here on differences in elevation parameters near segment ends, where melt entrainment effects should be the most pronounced. Data for each first- and second-order discontinuity along slow- and intermediate-spreading ridges are presented in Tables 1 and 2, respectively.

[13] The study of *Carbotte et al.* [2004] compared ridge axis elevations at a uniform distance of

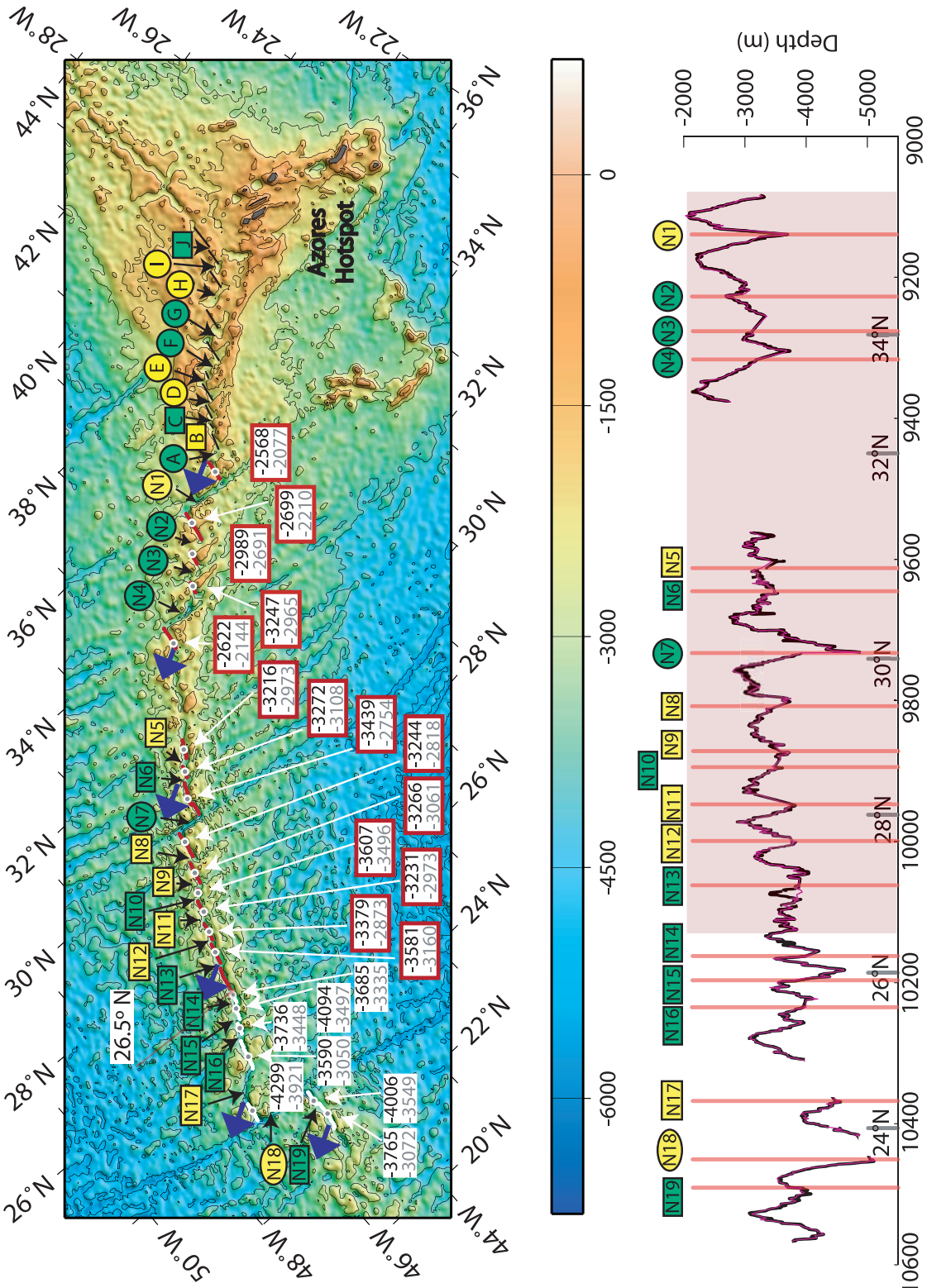


Figure 4

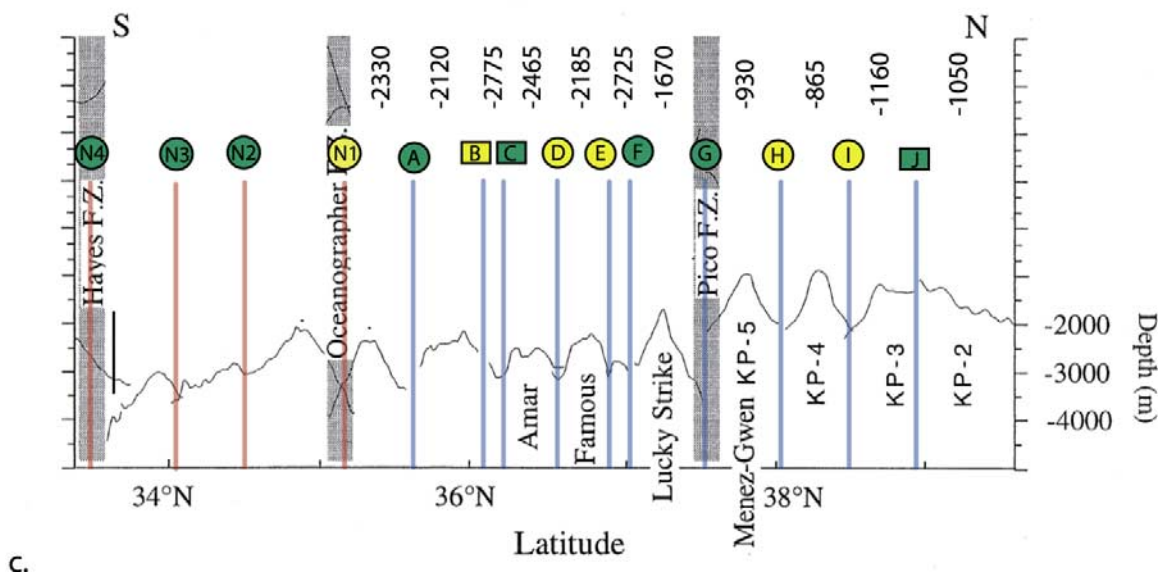


Figure 4. (continued)

10 km from a discontinuity. Closer than ~ 10 km, ridge axis structures that curve toward discontinuities often are observed and are believed to indicate influence of shear associated with the transform domain on ridge morphology [e.g., Phipps Morgan and Parmentier, 1984]. Here, we examine depth differences at a range of distances from segment ends to assess the sensitivity of results to a chosen reference distance. In most cases, results obtained at 5 and 15 km are consistent with the 10 km data set (90% of cases for the intermediate-spreading ridge segments and 82% of the slow-spreading cases, Tables 1 and 2).

[14] Portions of the ridge with geochemical and geophysical anomalies consistent with the influence of a nearby hot spot are grouped separately in

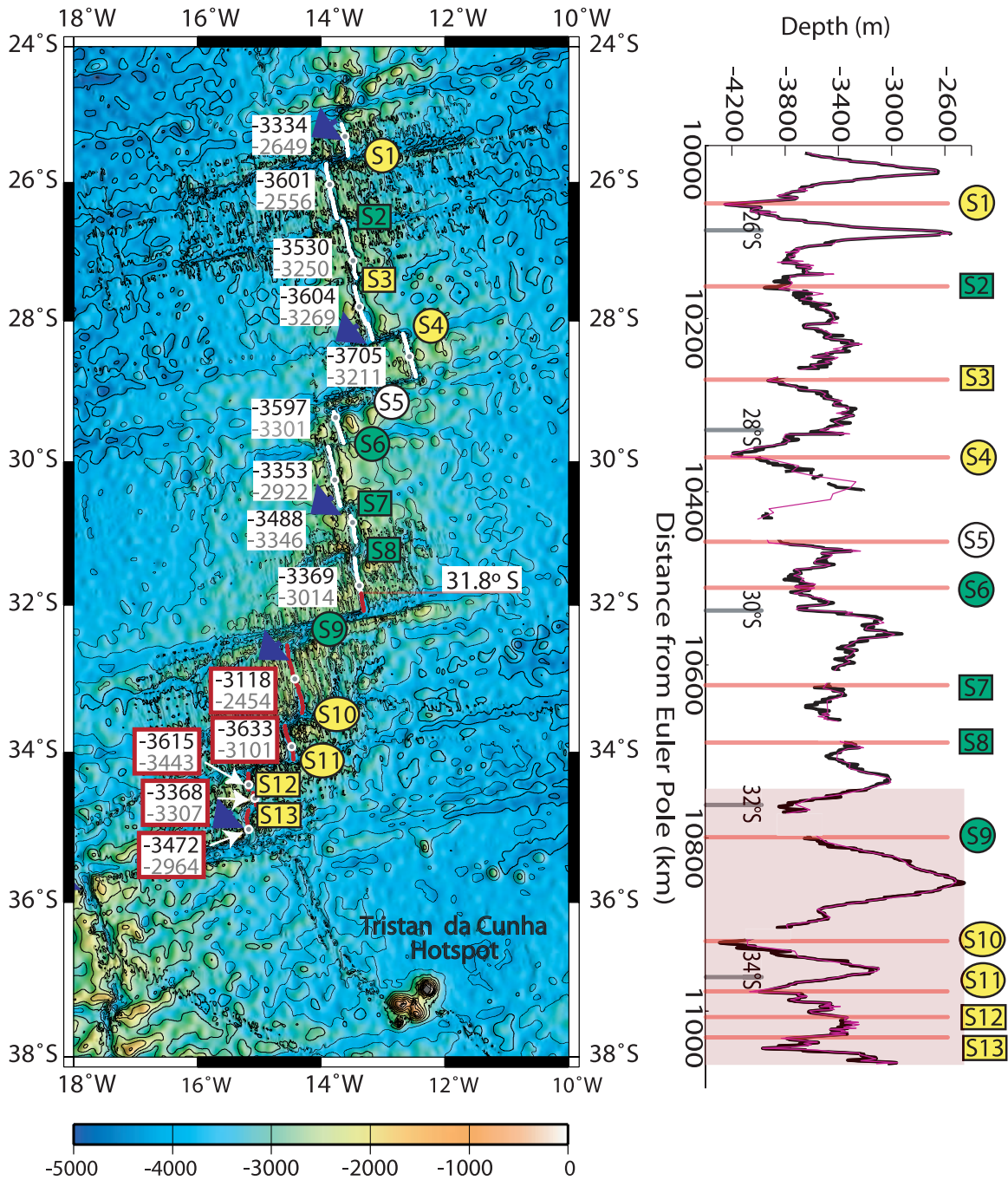
our analysis as hot spot-influenced segments and those devoid of such anomalies will be referred to as normal segments. For many MORs in proximity to hot spots, the extent of hot spot influence is actively debated. For the purposes of our analyses, we adopt one definition for each region based primarily on the existing geochemical studies.

3. Results

3.1. Slow-Spreading Centers

[15] Our study area of the NMAR extends from 22° – 36° N within which bathymetric data coverage is adequate to image 21 segments offset by six first-order and 13 second-order discontinuities

Figure 4. (a) Bathymetric map of the NMAR. The ridge axis is identified in red where geochemical evidence supports influence of the Azores hot spot (assumed to extend north of $\sim 26.5^{\circ}$ N on the basis of results of Klein and Langmuir [1989] and Thibaud *et al.* [1998]) and white elsewhere. Numbered circles and squares positioned above the ridge correspond with first-order discontinuities (transform faults) and second-order discontinuities (nontransform offsets), respectively. Green backgrounds signify the leading segment is shallower, and yellow backgrounds signify the trailing segment is shallower at a distance of 10 km from each offset. Below the axis, for each segment a white box displays the average depth (black) and the shallowest depth in meters (gray). Red outlined boxes denote hot spot-influenced segments. Blue arrows are ridge migration vectors ranging from ~ 21 mm/year in the north to ~ 20 mm/year in the south, with respect to the hot spot reference frame [Small and Danyushevsky, 2003]. (b) Axial depth profile of the NMAR 36° – 22° N plotted versus distance from the Euler pole (NUVEL-1A [DeMets *et al.*, 1994]). Digitized axis picks are in purple, and smoothed axis picks using a box filter of 400 m across axis and 1 km along axis are shown in black. First- and second-order discontinuities are marked by pink lines with the offset numbers labeled. (c) Along-axis variations in seafloor depth for the NMAR between 33.5° N and 40° N from Thibaud *et al.* [1998] (black segments in Figure 4a). Depth asymmetries across discontinuities are estimated from this profile for the region north of the Oceanographer FZ where multibeam bathymetry data are not publicly available. First- and second-order discontinuities for this region are labeled alphabetically, and segment midpoint depths are shown above the profile.



a.

b.

Figure 5. (a) Bathymetric map and (b) axial depth profile of the SMAR 25°–35°S. The Tristan da Cunha hot spot influence on the SMAR is taken as extending south of ~31.8°S on the basis of geochemical analysis of *Humphris et al.* [1985]. North of offset S5 (label with white background), bathymetric coverage of the ridge axis is incomplete, and therefore the depth asymmetry across this offset cannot be calculated. Blue arrows are ridge migration vectors ranging from ~15 mm/year in the north to ~13 mm/year in the south, with respect to the hot spot reference frame [Small and Danyushevsky, 2003]. Other symbols are the same as in Figure 4.

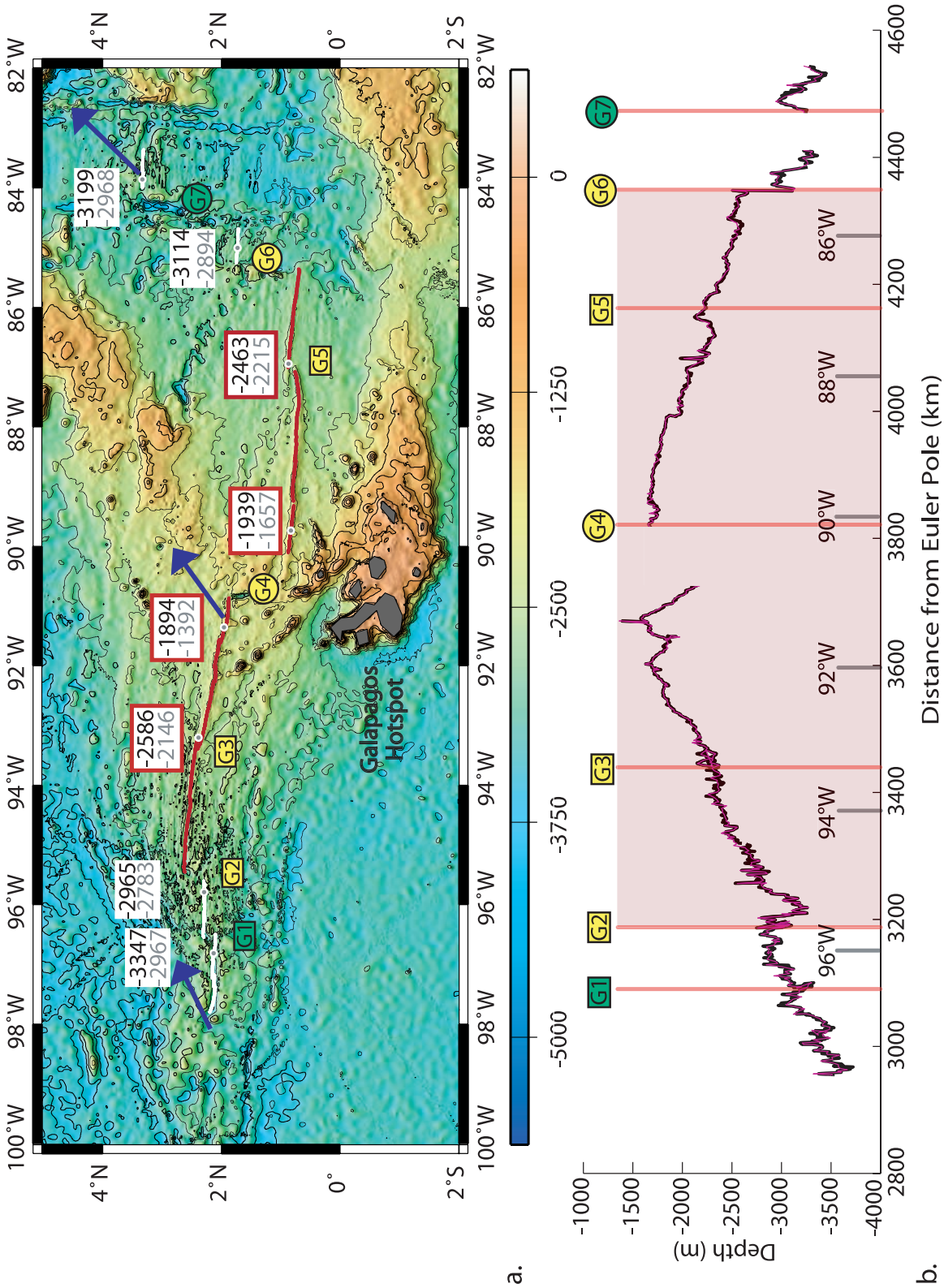


Figure 6

(Figures 4a and 4b). The full spreading rate within this region ranges from ~ 21 – 24 mm/year from north to south, with migration to the southwest at ~ 21 mm/year in the north and ~ 20 mm/year in the south [DeMets *et al.*, 1994; Small and Danyushevsky, 2003]. The Azores hot spot lies ~ 100 km east of the NMAR at a latitude of $\sim 39^\circ\text{N}$ and influences the structure and geochemistry of the ridge for 100s of km to the north and south. La/Sm ratios measured in ridge axis basalts [Schilling *et al.*, 1983] indicate the mantle source signature of the Azores hot spot extends to the Hayes Fracture Zone (Figure 4 offset N4). This interpretation is supported by the more recent geochemical study of Debaille *et al.* [2006], which identifies a transition from E-MORB to N-MORB coincident with N4. However, the thermal effect of the Azores hot spot on the depth and extent of melting beneath the NMAR may extend much further to the south. Klein and Langmuir [1989] observed a change in the along axis gradient of $\text{Fe}_{8,0}^G$ and $\text{Si}_{8,0}^G$ values (which represent Fe and Si normalized to 8 wt% MgO with local variability removed) in ridge axis basalts at $26^\circ 30'\text{N}$, with higher values to the north attributed to elevated mantle temperatures and hence deeper and greater extents of melt beneath the ridge axis. Long-wavelength gradients are observed along the NMAR in both ridge axis depths and Mantle Bouguer Anomalies (MBA) with average depths increasing and MBA increasing (becoming less negative) from the Azores platform to the south [Thibaud *et al.*, 1998]. Thibaud *et al.* [1998] attributes the coincidence of these bathymetric and MBA trends along with the geochemical trends to a long wavelength thermal anomaly from the Azores hot spot that extends 1600 km south to $\sim 26^\circ 30'\text{N}$. This southern limit lies within the middle of the segment north of offset N14 (Figure 4). Although there is clearly uncertainty regarding the southern limit of Azores hot spot influence, we use here this maximum extent supported by the Thibaud *et al.* [1998] and Klein and Langmuir [1989] studies. Multibeam bathymetric data are not publicly available for the NMAR proximal to the Azores hot spot north of 36°N . For this region we include axial depths estimated from the bathymetric profile published by Thibaud *et al.* [1998] (Figure 4c). These data

extend to 40°N and encompass an additional seven first-order and three second-order discontinuities. Segment endpoint depths for this region are estimated from an axial profile without the spatial averaging carried out for the rest of the study area. However, our tests of varying spatial filters indicate that while the magnitude of depth differences measured across discontinuities varies with filter width (e.g., Figure 3), the sense of depth asymmetry (i.e., which segment is shallower), which is of most interest in this study, remains consistent.

[16] Our study area of the SMAR extends from 25 – 35°S within which adequate bathymetric coverage is available for 14 segments offset by seven first-order and six second-order discontinuities (Figure 5). In this region, the SMAR spreads at a full rate of ~ 34 mm/year and is migrating to the southwest at a rate of ~ 15 mm/year in the north and ~ 13 mm/year in the south [DeMets *et al.*, 1994; Small and Danyushevsky, 2003]. The Tristan da Cunha hot spot lies ~ 450 km east of the axis of the SMAR, at a latitude of $\sim 37^\circ\text{S}$ and presently is not associated with prominent bathymetric or MBA anomalies along the SMAR [Ito and Lin, 1995a]. Fontignie and Schilling [1996] have proposed that the Tristan plume was a center of injection for broad-scale pollution of the asthenosphere, with Pb-Nd-Sr isotopic ratios from segments between 24°S and 47°S tending toward the field of the Tristan hot spot. Humphris *et al.* [1985] argued that on the basis of the presence of basalts with high K_2O contents (>0.18 wt%) and high ratios of Nb/Zr (>0.05), $(\text{La}/\text{Sm})_N$ (>0.8) and $(\text{Ce}/\text{Yb})_N$ (>1.1), the Tristan da Cunha hot spot appears to affect the MAR irregularly between $37^\circ 11'\text{S}$ and $31^\circ 50'\text{S}$. The Humphris *et al.* [1985] hot spot influence definition is used in this analysis which includes our offsets S9–S13 (Figure 5).

[17] Differences in axial depth of MAR segments measured at 10 km from each discontinuity (Table 1) are plotted as a function of discontinuity offset length in Figure 8. Numbered and lettered discontinuities correspond to those identified in Figures 4 and 5. Hot spot–influenced segments are plotted separately from normal segments as described above. Both the Azores and Tristan da Cunha hot spots are located east of the current

Figure 6. (a) Bathymetric map and (b) axial depth profile of the GSC 83° – 98°W . The Galápagos hot spot influence on the GSC, as identified from geochemical and geophysical indicators, extends between 95.5°W (offset G2) and 85°W (offset G6). Blue arrows are ridge migration vectors ranging from ~ 42 mm/year in the west to ~ 54 mm/year in the east, with respect to the hot spot reference frame [Small and Danyushevsky, 2003]. Other symbols are the same as in Figure 4.

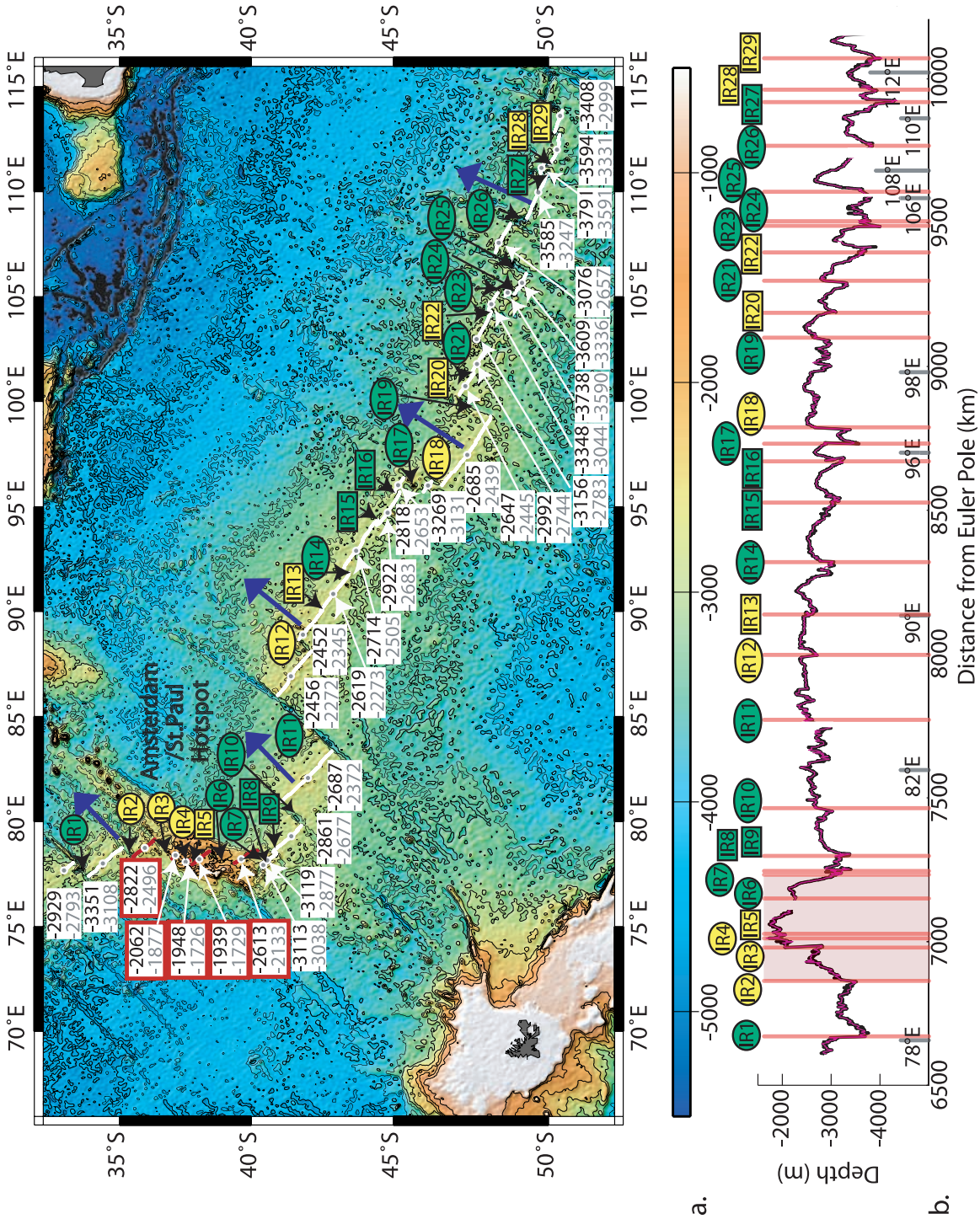


Table 1. Differences in Elevation Parameters Across Discontinuities for Slow-Spreading Segments

Offset Number ^a	Offset Length, ^b km	Seg. Length, km, North of Offset	Seg. Length, km, South of Offset	Depth Difference, m, at 5 km ^c	Depth Difference, m, at 10 km ^c	Depth Difference, m, at 15 km ^c
<i>NMAR</i>						
<i>J</i>	-5	70	50	<i>NA</i>	250	<i>NA</i>
<i>I</i>	-42 ^T	50	53	<i>NA</i>	-180	<i>NA</i>
<i>H</i>	-108 ^T	53	54	<i>NA</i>	-140	<i>NA</i>
<i>G</i>	-83 ^T	54	58	<i>NA</i>	1420	<i>NA</i>
<i>F</i>	-75 ^T	58	19	<i>NA</i>	150	<i>NA</i>
<i>E</i>	-36 ^T	19	40	<i>NA</i>	-10	<i>NA</i>
<i>D</i>	-41 ^T	40	47	<i>NA</i>	-105	<i>NA</i>
<i>C</i>	-24	47	18	<i>NA</i>	25	<i>NA</i>
<i>B</i>	-20	18	53	<i>NA</i>	-230	<i>NA</i>
<i>A</i>	-73 ^T	53	52	<i>NA</i>	455	<i>NA</i>
<i>N1</i>	-123 ^T	52	79	774	654	425
<i>N2</i>	-39 ^T	79	39	-84	-255	15
<i>N3</i>	-37 ^T	39	30	-64	-66	84
<i>N4</i>	-116 ^T	30	61	-422	-284	-290
<i>N5</i>	-17	49	31	-297	34	23
<i>N6</i>	-12	31	90	-182	-62	-48
<i>N7</i>	-71 ^T	90	71	-559	-859	-746
<i>N8</i>	-14	71	57	-327	153	142
<i>N9</i>	-12	57	15	282	254	354
<i>N10</i>	-9	15	42	-23	-241	-330
<i>N11</i>	-13	42	48	642	664	223
<i>N12</i>	-8	48	56	287	174	105
<i>N13</i>	-7	56	99	52	-421	-493
<i>N14</i>	-6	99	35	-374	-20	434
<i>N15</i>	-10	35	30	-663	-845	-871
<i>N16</i>	-11	30	80	-99	-228	131
<i>N17</i>	-59	80	51	622	684	644
<i>N18</i>	147 ^T	51	40	126	-195	-331
<i>N19</i>	7	40	77	291	351	122
<i>SMAR</i>						
<i>S1</i>	-38 ^T	54	91	233	252	232
<i>S2</i>	7	91	96	<i>NA</i>	198	-22
<i>S3</i>	-6	96	89	191	164	-24
<i>S4</i>	49 ^T	89	72	-236	-289	-152
<i>S5</i>	-138 ^T	72	52	-372	<i>NA</i>	<i>NA</i>
<i>S6</i>	-23 ^T	52	95	75	-135	-214
<i>S7</i>	12	95	42	-38	54	114
<i>S8</i>	-8	42	83	-167	-131	-124
<i>S9</i>	-127 ^T	83	105	-208	-284	-432
<i>S10</i>	-33 ^T	105	53	429	520	393
<i>S11</i>	-72 ^T	53	25	22	382	309
<i>S12</i>	7	25	20	-114	-163	-283
<i>S13</i>	-13	20	30	160	507	297

^a Lettered offsets refer to data from *Thibaud et al.* [1998].

^b Discontinuity offset length measured as perpendicular distance between two bounding segments. Sign convention adopted here is positive offset length indicates northern bounding segment is offset in the direction of ridge migration and positive axis depth difference indicates northern bounding segment is shallower (see Figure 1). Superscript "T" indicates transform faults.

^c Bold indicates leading segments are shallower. Italic indicates at least one bounding segment is hot spot-influenced. NA, not available.

Figure 7. (a) Bathymetric map and (b) axial depth profile of the SEIR 77°–114°E. Between 35.5°S (offset IR2) and 40.2°S (offset IR7) the ridge axis has a geochemical signature of the Amsterdam/St. Paul hot spot. Blue arrows are ridge migration vectors ranging from ~36 mm/year in the northwest to ~47 mm/year in the southeast, with respect to the hot spot reference frame [*Small and Danyushevsky*, 2003]. Other symbols are the same as in Figure 4.

Slow-Spreading NMAR & SMAR Data

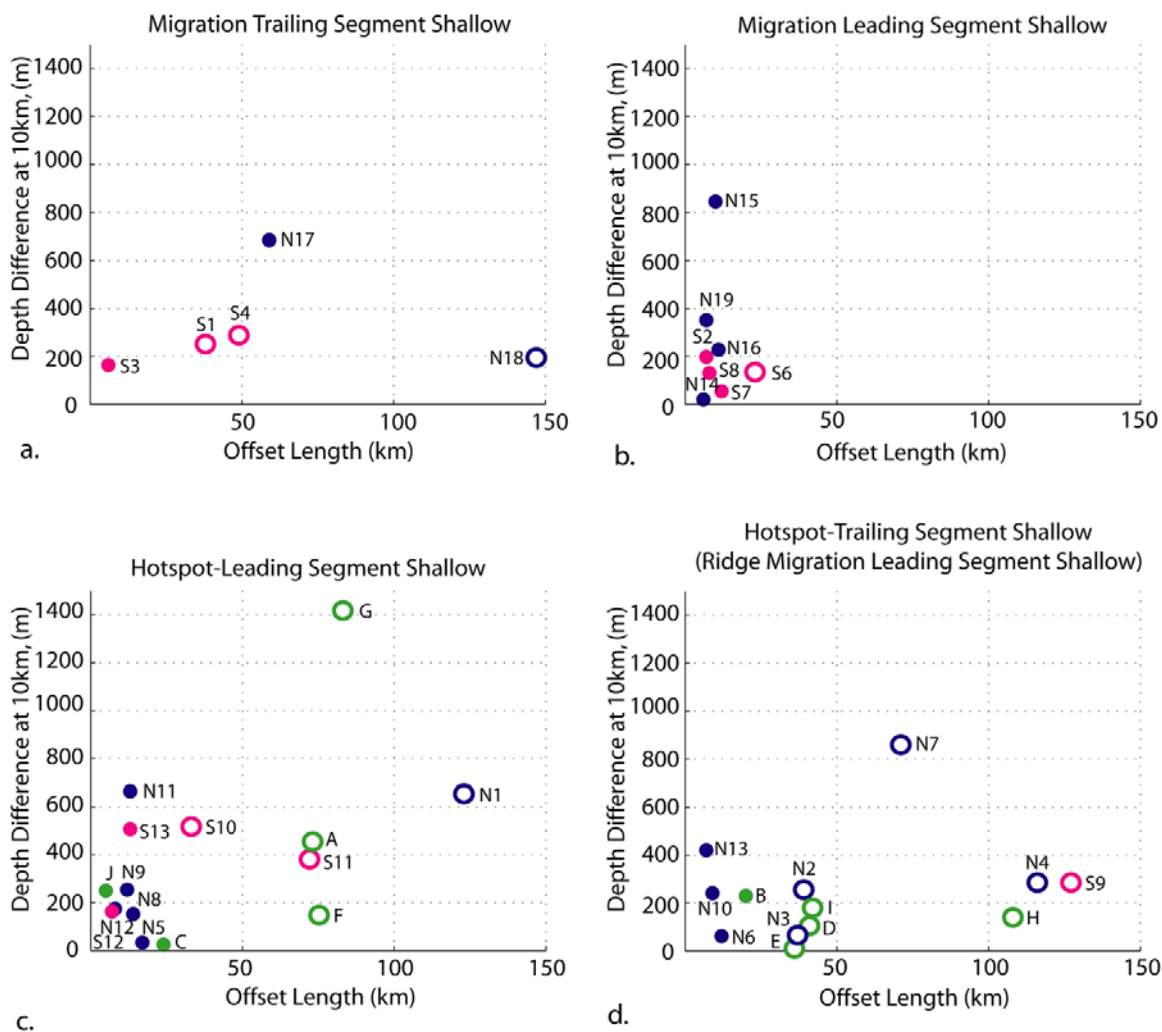


Figure 8. Differences in axial depth at 10 km from each offset versus discontinuity offset length for the slow-spreading SMAR (pink), NMAR (blue), and *Thibaud et al.* [1998] NMAR data (green). Transform faults are indicated by large open symbols. Data plotted correspond with absolute values of data in Table 1 and are grouped into all cases where (a) the trailing segment is shallower and (b) the leading segment is shallow. Data for hot spot–influenced segments are in (c) hot spot–leading segments shallower and (d) hot spot–trailing segments shallower.

MAR axis, which migrates in the opposite direction, to the southwest. Therefore those hot spot–influenced ridge segments that are offset opposite the direction of ridge migration (trailing) step toward the hot spots and are referred to here as hot spot–leading segments (Figure 1). For normal segments, leading segments are shallower at 25% of transform offsets (1 of 4) and 78% of nontransform offsets (7 of 9). Offset S5 is excluded from this analysis due to incomplete bathymetric coverage of the ridge axis. For hot spot–influenced portions of the MAR, hot spot–leading segments are shallower across 40% of transform offsets (6 of

15) and 69% of nontransform offsets (9 of 13). Similar results are obtained if other interpretations of the extent of hot spot influence along the MAR are assumed. For example, if Azores hot spot influence on the SMAR extends throughout the study area, then leading segments are shallower at 53% (8/15) of all discontinuities for non-hot spot–influenced MAR and hot spot–leading segments are shallower for 50% (13/26) of discontinuities along hot spot–influenced MAR (see Table 1).

Table 2. Differences in Elevation Parameters Across Discontinuities for Intermediate-Spreading Segments

Offset Number	Offset Length, ^a km	Seg. Length West of Offset, km	Seg. Length East of Offset, km	Depth Difference, m, at 5 km ²	Depth Difference, m, at 10 km ^b	Depth Difference, m, at 15 km ^b
<i>GSC</i>						
G1	23	146	106	217	129	108
G2	22	<i>106</i>	<i>256</i>	<i>-54</i>	<i>-232</i>	<i>-220</i>
G3	-7	<i>256</i>	<i>287</i>	<i>-9</i>	<i>41</i>	<i>-11</i>
G4	<i>-102^T</i>	<i>287</i>	<i>337</i>	<i>396</i>	<i>321</i>	<i>241</i>
G5	25	<i>337</i>	<i>185</i>	<i>-22</i>	<i>-96</i>	<i>-44</i>
G6	<i>159^T</i>	<i>185</i>	<i>64</i>	<i>-417</i>	<i>-332</i>	<i>-452</i>
G7	<i>130^T</i>	64	71	112	274	211
<i>SEIR</i>						
IR1	<i>-91^T</i>	57	192	-501	-702	-784
IR2	<i>-59^T</i>	<i>192</i>	<i>120</i>	<i>310</i>	<i>282</i>	<i>211</i>
IR3	<i>-115^T</i>	<i>120</i>	<i>29</i>	<i>734</i>	<i>664</i>	<i>573</i>
IR4	<i>-50^T</i>	29	20	<i>191</i>	<i>14</i>	<i>-2</i>
IR5	<i>-19</i>	20	92	<i>180</i>	<i>99</i>	<i>40</i>
IR6	<i>-87^T</i>	92	<i>108</i>	-81	-100	-123
IR7	<i>-67^T</i>	<i>108</i>	<i>12</i>	<i>240</i>	<i>-26</i>	<i>NA</i>
IR8	5	12	65	105	66	<i>NA</i>
IR9	15	65	156	95	42	30
IR10	<i>124^T</i>	156	279	267	240	184
IR11	<i>311^T</i>	279	109	249	250	258
IR12	<i>67^T</i>	109	151	-300	-351	-331
IR13	5	151	184	-141	-109	-209
IR14	<i>32^T</i>	184	226	268	284	320
IR15	-14	226	154	-8	-54	-20
IR16	24	154	62	188	237	313
IR17	<i>-89^T</i>	62	50	-618	-543	-440
IR18	<i>-37^T</i>	50	304	650	636	677
IR19	<i>140^T</i>	304	95	177	301	308
IR20	8	95	104	-46	-64	-106
IR21	<i>44^T</i>	104	103	495	461	466
IR22	16	103	88	-92	-16	-177
IR23	<i>-25^T</i>	88	22	-339	-373	-382
IR24	<i>-20^T</i>	22	84	11	-127	-1
IR25	<i>130^T</i>	84	116	112	287	528
IR26	<i>-45^T</i>	116	164	-449	-501	-403
IR27	22	164	37	444	560	221
IR28	-20	37	106	71	6	29
IR29	17	106	78	3	-5	51

^aDiscontinuity offset length measured as perpendicular distance between bounding segments. Sign convention adopted here is positive offset length indicates eastern bounding segment is offset in the direction of ridge migration and positive axis depth difference indicates eastern bounding segment is shallower (see Figure 1). Superscript “T” indicates transform faults.

^bBold indicates leading segments are shallower. Italic indicates at least one bounding segment is hot spot–influenced. NA, not available.

3.2. Intermediate-Spreading Centers

[18] The GSC spreads at a full rate that ranges from ~45 to ~66 mm/year and migrates to the northeast at a rate of ~42 to ~54 mm/year across the study area (98°W to 83°W) (Figure 6) [DeMets et al., 1994; Small and Danyushevsky, 2003]. Within this region there are eight segments offset by three first-order and four second-order discontinuities. The ridge axis comes closest to the Galápagos hot spot and reaches its shallowest depth near 91°W, which is ~200 km north of the Galápagos Archipelago, whose western end marks the probable center of the Galápagos mantle plume [White et al., 1993;

Sinton et al., 2003]. Detailed studies indicate a boundary in major element geochemistry coincident with the 95.5°W propagator, with normal MORB found west of this discontinuity [Christie and Sinton, 1981; Hey et al., 1989; Cushman et al., 2004]. Between 95.5°W (offset G2) and 85°W (offset G6), GSC lavas are classified as either “transitional” ($0.09 < K/Ti < 0.15$) or “enriched” MORB ($K/Ti > 0.15$) and are indicative of Galápagos hot spot influence [Cushman et al., 2004; Christie et al., 2005]. Variations in trace element concentrations and trace element ratios, including La/Sm [Schilling et al., 1982] and radiogenic

isotopes [Schilling *et al.*, 2003], also indicate geochemical boundaries roughly coincident with the 95.5°W and 85°W discontinuities. Gravity and seismic studies indicate thicker crust and support hot spot influence within this region [Ito and Lin, 1995b; Detrick *et al.*, 2002; Canales *et al.*, 2002]. On the basis of these geochemical and geophysical indicators, the Galápagos hot spot influence appears to extend between offsets G2 and G6 (Figure 6).

[19] The SEIR has a full spreading rate that ranges from ~62 to ~72 mm/year and migrates to the northeast at a rate of ~36–47 mm/year across the study area (77°E to 114°E) (Figure 7) [DeMets *et al.*, 1994; Small and Danyushevsky, 2003]. This region encompasses 30 segments offset by 18 first-order and 11 second-order discontinuities, which includes the area from 100°–114°E originally included in the analysis of Carbotte *et al.* [2004]. Unlike the hot spots influencing the other regions investigated in this study, the Amsterdam-St. Paul (ASP) hot spot is nearly on-axis, with both the hot spot and portions of the SEIR axis sitting atop a ~30,000 km² plateau. The ASP hot spot volcanism was captured by the SEIR between 5 and 10 Ma and created a shallow platform by adding to the igneous accretion at the spreading center [Scheirer *et al.*, 2000]. Currently, the locus of ASP hot spot volcanism is within 40 km of the nearest spreading segments [Scheirer *et al.*, 2000]. Graham *et al.* [1999] report high ³He/⁴He ratios ranging between 9–13.4 R_A (R_A = atmospheric ratio) in basalts dredged from the ASP plateau (between offsets IR3 and IR7 ~ 37°S to 40.2°S). Such high ratios are interpreted to indicate material input from a mantle plume derived from a relatively undegassed (deep) source region [Graham *et al.*, 1999]. High ³He/⁴He ratios also are found along the ridge segment north of offset IR3, well to the north of the ASP plateau (up to 14.1 R_A). A sample collected from a short intratransform spreading center within offset IR2 shows normal MORB values (7–9 R_A) marking the northern boundary of ASP hot spot influence. Southeast of the ASP plateau (east of offset IR7), ridge axis basalts show ³He/⁴He values typical of normal MORB (7–9 R_A) [Graham *et al.*, 1999]. Furthermore, existing isotopic data provide no evidence that material derived from the ASP or the Kerguelen-Heard hot spots plays more than a minor role in the source mantle for the SEIR 86–118°E (offsets IR11 to IR29) [Mahoney *et al.*, 2002].

[20] Segment-to-segment elevation differences for the GSC and SEIR (Table 2) are plotted as a function of discontinuity offset length in Figure 9. Numbered discontinuities correspond to those identified in Figures 6 and 7. At these intermediate-spreading ridges, normal leading segments are shallower across 86% of transform offsets (12 of 14) and 55% of nontransform offsets (6 of 11) (Figures 9a and 9b). Depth anomalies across discontinuities vary with the offset length, with intersegment elevation differences generally increasing with discontinuity offset lengths of up to ~100 km and smaller elevation differences observed at the largest transform offsets (Figure 9b).

[21] As observed along the slow-spreading MAR, the Galápagos and ASP hot spots are offset from the ridge axis (only slightly in the case of Amsterdam/St. Paul) in the direction opposite ridge migration; therefore trailing segments in the ridge migration reference frame are hot spot–leading segments (Figure 1). When comparing ridge elevation at a distance of 10 km from each discontinuity, hot spot–leading segments are shallower at 100% of the transform (6 of 6) and nontransform offsets (4 of 4) (Figure 9c). Offset IR6 is excluded from this analysis because its bounding segments straddle the ASP hot spot. Hot spot proximity clearly dominates segment-scale ridge morphology at intermediate-spreading ridges; ridge segments offset toward a hot spot are, in all cases, shallower. Unlike the normal ridge segments, ridge axis depth differences between segments do not systematically increase with ridge offset length, and at larger offsets there is no apparent falloff in the magnitude of depth asymmetries (Figure 9c).

4. Discussion

4.1. Normal Segments

[22] Our analysis of the GSC and SEIR shows that, beyond the hot spot–influenced portions of these intermediate-spreading ridges, leading segments are shallower across 72% of first- and second-order discontinuities (86% of transform faults and 55% of second-order discontinuities). The probability of reaching these results by chance can be evaluated using a binomial model, with “success” for each trial (ridge-axis discontinuity) defined as having a shallower leading segment. Our assumptions are that the probability of success for each individual trial is $p = 0.5$ (as with a coin toss) and that each trial is independent. The odds of obtaining 18 of 25 successes by chance given these parameters are

Intermediate-Spreading GSC & SEIR Data

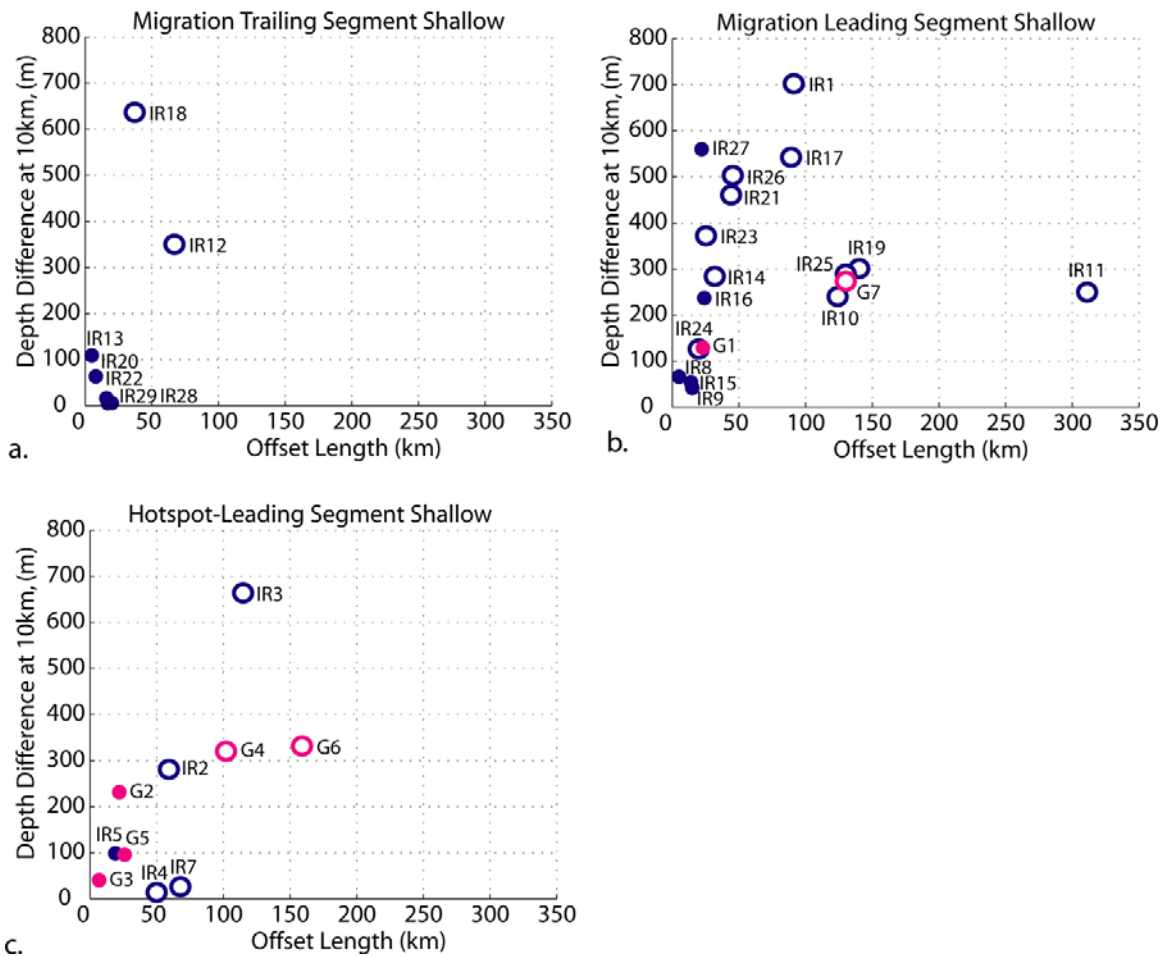


Figure 9. Differences in axial depth at 10 km from each offset versus discontinuity offset length for the intermediate-spreading GSC (pink) and SEIR (blue). Transform faults are indicated by large open symbols. Data plotted correspond with absolute values of data in Table 2 and are grouped into all cases where (a) the trailing segment is shallower and (b) the leading segment is shallow. Data for hot spot–influenced segments are in (c) hot spot–leading segments shallower and (d) hot spot–trailing segments shallower.

<2%. This significant correlation further supports the results of *Carbotte et al.* [2004] for fast- and intermediate-spreading MORs and indicates a strong correlation between ridge migration and ridge morphology at these spreading rates. Combined data from our study and *Carbotte et al.* [2004] show depth anomalies across discontinuities vary with the offset length of the discontinuity (Figure 10). These observations are consistent with predictions of numerical studies of ridge migration and asthenospheric flow [*Katz et al.*, 2004]. The *Katz et al.* [2004] model predicts that shear induced by migration of the lithosphere over the mantle produces a maximum asymmetry in melt production rates and potential crustal thickness at ~50–

100 km from the spreading axis. Hence, for isostatically compensated seafloor topography, this model predicts maximum depth asymmetries across ridge offsets of 50–100 km in length. In Figure 10, the predicted axis depth asymmetries of *Katz et al.* [2004] are shown for comparison with observations from both our study and *Carbotte et al.* [2004]. Although the data show considerable scatter, the general shape and amplitude of the *Katz et al.* [2004] curves fit the observations well. The prominent outlier is the Blanco transform fault of the intermediate-spreading Juan de Fuca Ridge. A very large change in axial depth occurs across this transform fault in part due to the Gorda Depression, which sits at the eastern end of the Blanco

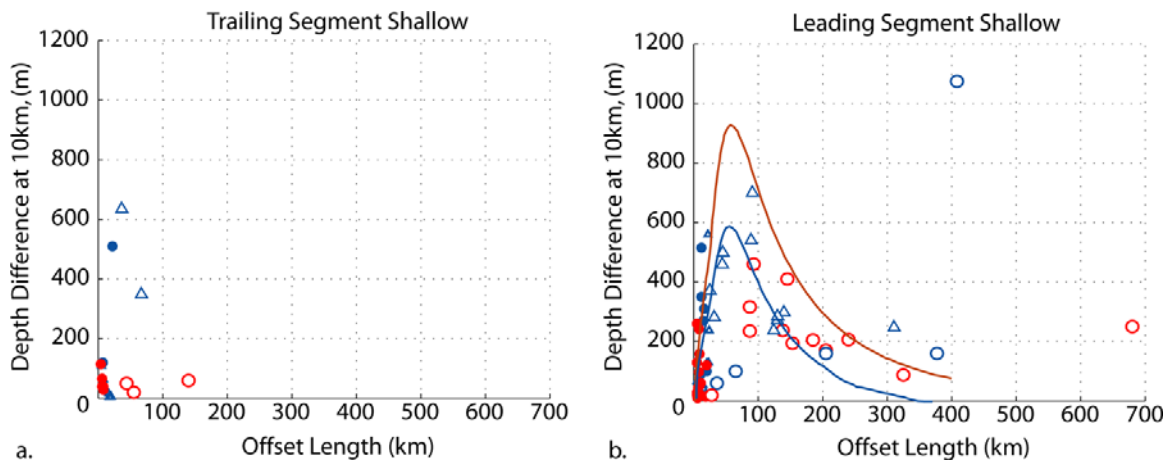


Figure 10. Global summary of ridge axis depth differences versus discontinuity offset lengths for fast- and intermediate-spreading ridges. Red circles show data for fast-spreading ridges (>80 mm/yr) from *Carbotte et al.* [2004]. Blue symbols show data for intermediate-spreading ridges (50–80 mm/yr); triangles are for GSC and SEIR data presented in this paper; and circles show data for other intermediate ridges from *Carbotte et al.* [2004]. Transform faults are indicated by larger open symbols. (a) Offsets with trailing segments shallower. (b) Offsets with leading segments shallower. Solid lines show model predictions from *Katz et al.* [2004] for a fast-spreading rate of 140 mm/year (red) and an intermediate-spreading rate of 60 mm/year (blue). The models predict maximum axial depth asymmetries for offset lengths of ~50–100 km and smaller asymmetries for larger offset transform faults.

transform fault zone and may have initially formed as the starting point of a northward propagating rift on the Gorda ridge system [*Embley and Wilson, 1992*].

[23] In contrast to results for fast- and intermediate-spreading ridges, a weaker correlation is observed between leading segments and shallow morphology along the slow-spreading MAR, where only 62% of leading segments (25% of transform faults and 78% of second-order discontinuities) are shallower at 10 km from the discontinuity. Assuming a binomial model with $p = 0.5$, the probability of reaching this result by chance is ~16%, which is not statistically significant. Although the public availability of ship-board multibeam data limits our analysis here to only 14 normal (non-hot spot-influenced) slow-spreading ridge segments, this result suggests that the relationship between ridge migration and melt delivery to the ridge axis is spreading-rate dependent. This spreading-rate dependence could reflect a more 3-D pattern of mantle upwelling and melt focusing at slow-spreading rates or the intermittent nature of magmatism and the significant role of tectonic extension on ridge morphology expected at these rates.

[24] Fast- and slow-spreading ridges differ markedly in the magnitude of along-axis gradients in ridge structure. Large gradients in gravity and seismic properties as well as km-scale variations in axial relief are observed within individual seg-

ments of slow-spreading ridges [e.g., *Lin et al., 1990; Tolstoy et al., 1993; Dunn et al., 2005*]. In contrast, fast spreading ridges exhibit only minor intrasegment changes in elevation (typically less than a few 100 m), smaller along-axis MBA anomalies and more uniform on-axis seismic structure [*Macdonald et al., 1988; Wang and Cochran, 1993; Detrick et al., 1987, 1993*]. These differences are thought to be manifestations of the deeper pattern of mantle upwelling beneath spreading centers. Numerical experiments have shown that buoyant upwelling beneath spreading centers, driven by thermal gradients and compositional density variations, should vary with spreading rate. An initial 2-D upwelling remains 2-D at high spreading rates; whereas, for low spreading rates, an initial 2-D structure transforms into a 3-D pattern [*Parmentier and Phipps Morgan, 1990; Sparks and Parmentier, 1993*]. Moreover, numerical models of stable 3-D flow solutions at slow-spreading rates become 2-D when the spreading rate is increased [*Choblet and Parmentier, 2001*]. Tomographic and electromagnetic studies along fast spreading ridges support the presence of a broad region of mantle upwelling and melt production consistent with passive flow and a quasi-2-D pattern of upwelling in this environment [e.g., *Forsyth et al., 1998; Evans et al., 1999*]. Conversely, the melt flux beneath a slow-spreading segment is greatest near the segment center, as evident from gravity and seismic studies [e.g., *Lin*

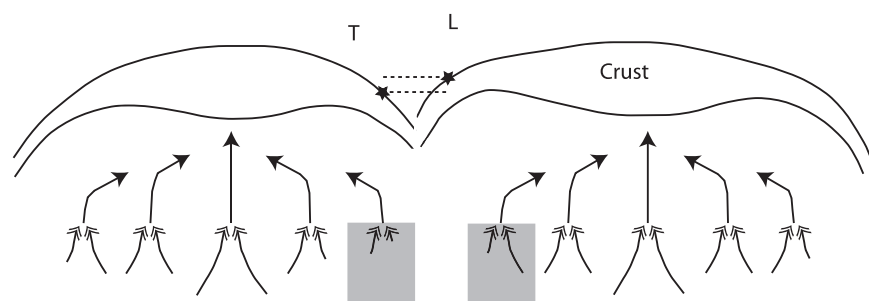


Figure 11. Cartoon of melt delivery beneath slow-spreading ridge segments. Double-headed arrows represent focusing of mantle melts beneath the ridge axis from a broad mantle melt source region. Single-headed arrows represent redistribution of melt to the crust. Stars indicate locations used for depth differences, with the leading segment at a shallower depth than the trailing segment (shown with dashed lines) at a distance of 10 km from the offset. As a result of 3-D upwelling and focusing of melts toward segment centers at slow-spreading ridges, little asymmetry in melt delivery to adjacent ridge segments due to ridge migration is expected. Idealized region of less melt availability at segment ends is shown in gray. See Figure 2b for similar along-axis profile view of melt delivery beneath a fast-spreading ridge.

et al., 1990; Tolstoy *et al.*, 1993; Dunn *et al.*, 2005] that indicate a thicker crust and/or hotter mantle in these regions. These centers of upwelling appear to be long-lived as evident by crenulated gravity patterns observed off-axis [Phipps Morgan and Parmentier, 1995]. The melt entrainment model of Carbotte *et al.* [2004] and Katz *et al.* [2004] assumes a broad region of 2-D mantle upwelling and melt production consistent with passive asthenospheric flow beneath ridges (Figure 2). Under the conditions of 3-D upwelling and melt focusing beneath segment centers that appear to exist at slow-spreading rates, segment ends receive a smaller percentage of the melt production associated with each segment compared to the fast spreading environment. Therefore, if melt tapping across discontinuities occurs at slow-spreading centers, we expect little melt availability for melt entrainment to the crust (Figure 11).

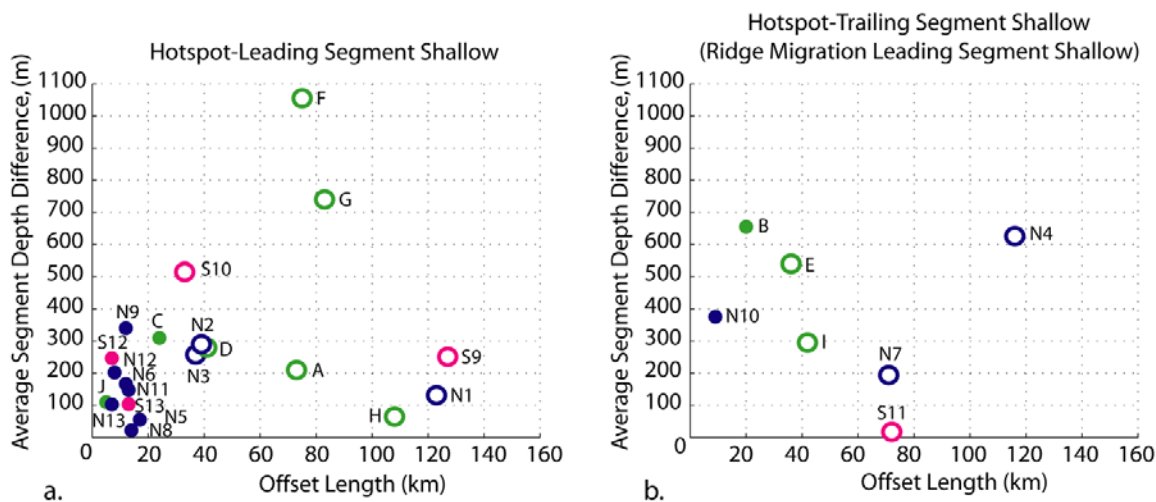
[25] In addition to patterns of melt delivery from the mantle, differences in the crustal level magmatic system also may contribute to the apparent spreading-rate dependence observed. Along the fast spreading East Pacific Rise, multichannel seismic studies image a nearly continuous crustal magma lens extending for tens of kilometers at a depth of ~ 1.2 – 2.4 km below the seafloor, suggesting its existence is relatively steady state [Detrick *et al.*, 1987, 1993]. Similarly, recent multichannel seismic work on the intermediate-spreading Juan de Fuca ridge shows that axial magma bodies also occur along more than 60% of the spreading axis at depths of ~ 2 – 2.5 km [e.g., Carbotte *et al.*, 2006]. In contrast, detection of magma bodies in the crust is rare in seismic data from slow-spreading centers and the shallow magmatic system appears to be

characterized by isolated magma bodies beneath segment centers that may be short-lived [e.g., Detrick *et al.*, 1990; Barclay *et al.*, 1998; Crawford *et al.*, 2005]. With intermittent magma delivery to the crust focused primarily to segment centers, ridge segment ends are strongly influenced by tectonic extension and axial depths may be dominated by the local history of tectonic stretching [e.g., Tucholke *et al.*, 1997]. Although our analysis does not include ultra-slow-spreading ridges, we expect 3-D segment scale effects to predominate in these environments as well.

4.2. Hot Spot–Influenced Segments

[26] Hot spot–ridge interaction is known to exert a long-wavelength influence on ridge bathymetry with shoaling toward axis-centered or near-axis hot spot sources observed in many locations [e.g., Ito *et al.*, 2003]. Our study of ridge morphology indicates that the effect of hot spot proximity varies with spreading rate. At the intermediate-spreading SEIR and GSC, segments stepping toward the hot spots are shallower in all cases; whereas, there is little correlation between hot spot–leading segments and depth asymmetries across discontinuities at the slow-spreading MAR. Here, for approximately half of the segment pairs examined, the segment closer to the hot spot is deeper not shallower across the discontinuity. Long-wavelength gradients along the ridge with hot spot proximity also differ markedly. Along the MAR, the axis shoals toward the Azores hot spot in a stepwise fashion with steps in ridge elevation or changes in depth gradients coincident with the major transform faults (e.g., Figure 4) [Thibaud *et al.*, 1998]. In contrast, axial depths shoal more continuously

Slow-Spreading NMAR & SMAR Data



Intermediate-Spreading GSC & SEIR Data

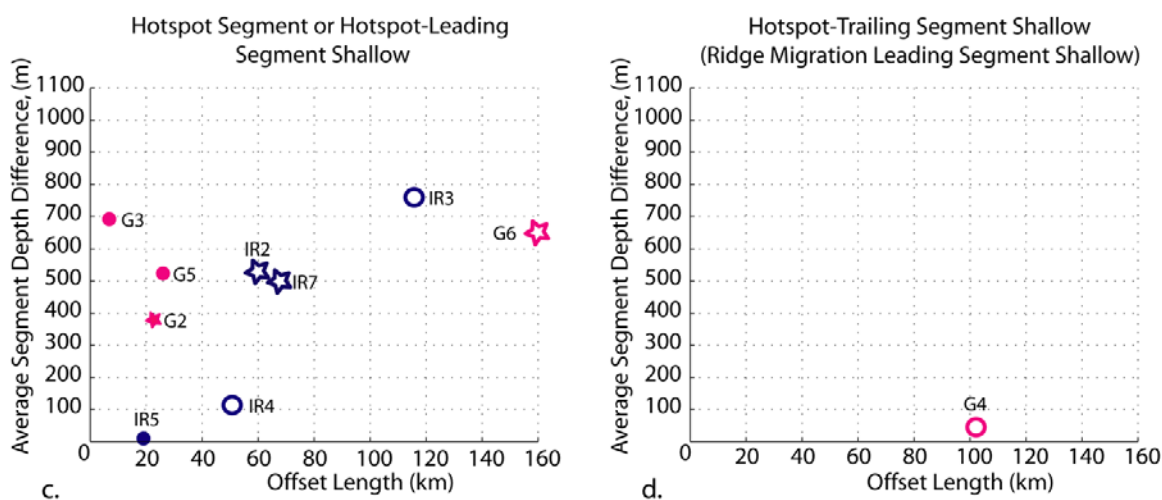


Figure 12. Difference in average axial depth for a ridge segment versus discontinuity offset length for all hot spot–influenced data. Color scheme follows Figures 8 and 9. Stars correspond with discontinuities bounded by a hot spot–influenced segment and a normal (non–hot spot–influenced) segment. Transform faults are indicated by large open symbols. Data for slow-spreading ridges are grouped into all cases where (a) the hot spot–leading segments are shallower and (b) the hot spot–trailing segments are shallower. Lettered offsets (green) correspond to axial depth at segment midpoints for NMAR north of Oceanography fracture zone estimated from *Thibaud et al.* [1998]. (c and d) Data for intermediate-spreading hot spot segments. At intermediate-spreading rates, for all cases where the discontinuity is bounded by one hot spot–influenced segment and one normal segment (stars in Figure 12c), the hot spot segment is shallower.

toward the Galápagos and ASP hot spots with only minor disruptions at discontinuities (Figures 6 and 7). This difference also is apparent in comparisons of average segment depths and hot spot proximity (Figure 12). Whereas almost all hot spot–leading segments are shallower at the intermediate-spreading ridges, hot spot proximity is not a consistent predictor of inter-segment elevation changes for the MAR.

[27] Three-dimensional fluid dynamic models of plume-ridge interaction predict differences in the channeling of plume material along a ridge as a function of spreading rate [*Albers and Christensen, 2001*], which could be related to these observed differences in ridge morphology. More pipe-like flow is expected at low spreading rates where the abruptly thickening lithosphere acts as an inverted channel to focus plume flow along axis. In con-

trast, more pancake like flow of plume material is predicted beneath faster spreading ridges. Continuous shoaling across discontinuities toward hot spots at intermediate-spreading ridges may arise from more pancake-like plume flow, where plume material and thermal inputs diminish radially from the plume source. We attribute the weaker correlation between depth asymmetries and hot spot proximity at slow-spreading centers to the dominant effects of 3-D mantle upwelling and segment-center melt focusing, as well as tectonic extension on segment end morphology. Fluid dynamic models predict that a number of factors in addition to spreading rate may influence hot spot–ridge interaction including ridge migration rate, hot spot flux, and ridge-hot spot separation distance [e.g., Ito *et al.*, 2003]. Observational constraints on the relative importance of these factors may be possible as a more complete bathymetric data set of the global MOR becomes available.

5. Summary

[28] Our study shows a much stronger correlation between ridge migration direction and axis morphology at fast- and intermediate-spreading ridges, as compared to slow-spreading ridges. The correlation is greatest across transform faults where segments offset in the direction of ridge migration are consistently shallower than neighboring trailing segments. Globally, fast- and intermediate-spreading MORs show a correlation between migration direction and axial morphology that supports a melt entrainment model invoking asymmetric mantle upwelling due to ridge migration and across-discontinuity melt tapping [Carbotte *et al.*, 2004]. A relationship between axial depth differences across discontinuities and offset lengths also is supported by this analysis, with maximum depth anomalies observed at the critical offset length of 50–100 km, as predicted by Katz *et al.* [2004]. We attribute the weaker correlation between ridge migration and axial depths at slow-spreading rates to enhanced 3-D upwelling and melt focusing to segment centers that limits the entrainment of melt from across the discontinuity. For hot spot–influenced portions of the MOR, hot spot proximity dominates ridge morphology at intermediate-spreading centers but is not a consistent predictor of axial depth asymmetries between segments at slow-spreading centers. These results could reflect spreading-rate-dependent differences in the channeling of hot spot material to ridges, as well as the predominance of 3-D upwelling and

segment-center melt focusing in the slow-spreading environment.

Acknowledgments

[29] We greatly appreciate the thoughtful reviews of Bruce Luyendyk, Tanya Atwater, and Del Bohlenstiehl. Ridge axial picks kindly were provided by Jim Cochran and Dan Scheirer. Plate kinematic data were contributed by Chris Small. The project was funded in part by NSF OCE–0324668, NOAA/NA040AR600049, NSF OCE-9816021, NSF OCE-0526942.

References

- Albers, M., and U. L. Christensen (2001), Channeling of plume flow beneath mid-ocean ridges, *Earth Planet. Sci. Lett.*, *187*, 207–220.
- Barclay, A. H., D. R. Toomey, and S. C. Solomon (1998), Seismic structure and crustal magmatism at the Mid-Atlantic Ridge, 35°N, *J. Geophys. Res.*, *103*(B8), 17,827–17,844.
- Canales, J. P., J. J. Dañobeitia, R. S. Detrick, E. E. E. Hooft, R. Bartolomé, and D. F. Naar (1997), Variations in axial morphology along the Galápagos spreading center and the influence of the Galápagos hotspot, *J. Geophys. Res.*, *102*(B12), 27,341–27,354.
- Canales, J. P., G. Ito, R. S. Detrick, and J. Sinton (2002), Crustal thickness along the western Galápagos Spreading Center and the compensation of the Galápagos hotspot swell, *Earth Planet. Sci. Lett.*, *203*, 311–327.
- Carbotte, S. M., and K. C. Macdonald (1994), Comparison of seafloor tectonic fabric at intermediate, fast, and super fast spreading ridges: Influence of spreading rate, plate motions, and ridge segmentation on fault patterns, *J. Geophys. Res.*, *99*(B7), 13,609–13,632.
- Carbotte, S. M., C. Small, and K. Donnelly (2004), The influence of ridge migration on the magmatic segmentation of mid-ocean ridges, *Nature*, *429*, 743–746.
- Carbotte, S. M., R. S. Detrick, A. Harding, J. P. Canales, J. Babcock, G. Kent, E. Van Ark, M. Nedimovic, and J. Diebold (2006), Rift topography linked to magmatism at the intermediate spreading Juan de Fuca Ridge, *Geology*, *34*(3), 209–212.
- Choblet, G., and E. M. Parmentier (2001), Mantle upwelling and melting beneath slow spreading centers: Effects of variable rheology and melt productivity, *Earth Planet. Sci. Lett.*, *184*, 589–604.
- Christie, D. M., and J. M. Sinton (1981), Evolution of abyssal lavas along propagating segments of the Galápagos Spreading Center, *Earth Planet. Sci. Lett.*, *56*, 321–335.
- Christie, D. M., R. Werner, F. Hauff, K. Hoernle, and B. B. Hanan (2005), Morphological and geochemical variations along the eastern Galápagos Spreading Center, *Geochem. Geophys. Geosyst.*, *6*, Q01006, doi:10.1029/2004GC000714.
- Cochran, J. R., J. Sempéré, and SEIR Scientific Team (1997), The Southeast Indian Ridge between 88°E and 118°E: Gravity anomalies and crustal accretion at intermediate spreading rates, *J. Geophys. Res.*, *102*(B7), 15,463–15,487.
- Crawford, W. C., et al. (2005), Preliminary results from the SISMOMAR seismic study of the Lucky Strike Segment, 37°N Mid-Atlantic Ridge, *Eos Trans. AGU*, *86*(52), Fall Meet. Suppl., Abstract T31B-0506.
- Cushman, B., J. Sinton, G. Ito, and J. Eaby Dixon (2004), Glass compositions, plume-ridge interaction, and hydrous melting along the Galápagos Spreading Center, 90.5°W

- to 98°W, *Geochem. Geophys. Geosyst.*, 5, Q08E17, doi:10.1029/2004GC000709.
- Darbyshire, F. A., R. S. White, and K. F. Priestley (2000), Structure of the crust and uppermost mantle of Iceland from a combined seismic and gravity study, *Earth Planet. Sci. Lett.*, 181, 409–428.
- Davis, E. E., and J. L. Karsten (1986), On the cause of the asymmetric distribution of seamounts about the Juan de Fuca Ridge: Ridge-crest migration over a heterogeneous asthenosphere, *Earth Planet. Sci. Lett.*, 79, 385–396.
- Debaille, V., J. Blichert-Toft, A. Agranier, R. Doucelance, P. Schiano, and F. Albarede (2006), Geochemical component relationships in MORB from the Mid-Atlantic Ridge, 22–35 degrees N, *Planet. Sci. Lett.*, 241, 844–862.
- DeMets, C., R. G. Gordon, D. F. Argus, and S. Stein (1994), Effect of recent revisions to the geomagnetic reversal time scale on estimate of current plate motions, *Geophys. Res. Lett.*, 21(20), 2191–2194.
- Detrick, R. S., P. Buhl, E. Vera, J. Mutter, J. Orcutt, J. Madsen, and T. Brocher (1987), Multi-channel seismic imaging of a crustal magma chamber along the East Pacific Rise, *Nature*, 326, 35–41.
- Detrick, R. S., J. C. Mutter, P. Buhl, and I. I. Kim (1990), No evidence from multichannel reflection data for a crustal magma chamber in the MARK area on the Mid-Atlantic Ridge, *Nature*, 347, 61–64.
- Detrick, R. S., A. J. Harding, G. M. Kent, J. A. Orcutt, J. C. Mutter, and P. Buhl (1993), Seismic structure of the southern East Pacific Rise, *Science*, 259, 499–503.
- Detrick, R. S., J. M. Sinton, G. Ito, J. P. Canales, M. Behn, T. Blacic, B. Cushman, J. E. Dixon, D. W. Graham, and J. J. Mahoney (2002), Correlated geophysical, geochemical, and volcanological manifestations of plume-ridge interaction along the Galápagos Spreading Center, *Geochem. Geophys. Geosyst.*, 3(10), 8501, doi:10.1029/2002GC000350.
- Dunn, R. A., V. Lekić, R. S. Detrick, and D. R. Toomey (2005), Three-dimensional seismic structure of the Mid-Atlantic Ridge (35°N): Evidence for focused melt supply and lower crustal dike injection, *J. Geophys. Res.*, 110, B09101, doi:10.1029/2004JB003473.
- Embley, R. W., and D. S. Wilson (1992), Morphology of the Blanco Transform fault zone-NE Pacific: Implications for its tectonic evolution, *Mar. Geophys. Res.*, 14(1), 25–45.
- Evans, R. L., et al. (1999), Asymmetric electrical structure in the mantle beneath the East Pacific Rise at 17°S, *Science*, 286, 752–756.
- Fontignie, D., and J.-G. Schilling (1996), Mantle heterogeneities beneath the South Atlantic: A Nd-Sr-Pb isotope study along the Mid-Atlantic Ridge (3°S–46°S), *Earth Planet. Sci. Lett.*, 142, 209–221.
- Forsyth, D. W., et al. (1998), Imaging the deep seismic structure beneath a mid-ocean ridge: The MELT experiment, *Science*, 280, 1215–1218.
- Fox, P. J., N. R. Grindlay, and K. C. MacDonald (1991), The Mid-Atlantic Ridge (31°S–34°30'S): Temporal and spatial variations of accretionary processes, *Mar. Geophys. Res.*, 13(1), 1–20.
- Gente, P., R. Pockalny, C. Durand, C. Deplus, M. Maia, G. Ceuleneer, C. Mevel, and C. Laverne (1995), Characteristics and evolution of the segmentation of the Mid-Atlantic Ridge between 20°N and 24°N during the last 10 Myr, *Earth Planet. Sci. Lett.*, 129, 55–71.
- Graham, D. W., K. T. M. Johnson, L. D. Priebe, and J. E. Lupton (1999), Hotspot-ridge interaction along the Southeast Indian Ridge near Amsterdam and St. Paul Islands: Helium isotope evidence, *Earth Planet. Sci. Lett.*, 167, 297–310.
- Grindlay, N. R., J. P. Fox, and K. C. MacDonald (1991), Second-order ridge axis discontinuities in the South Atlantic: Morphology, structure, and evolution, *Mar. Geophys. Res.*, 13(1), 21–49.
- Haxby, W. F., W. B. Ryan, and S. M. Carbotte (2003), The MapApp Virtual Seabed Explorer, *Eos Trans. AGU*, 84(46), Fall Meet. Suppl., Abstract U22A-0023.
- Hey, R. N., M. C. Kleinrock, C. Martin, S. P. Miller, T. M. Atwater, and R. C. Searle (1986), Sea Beam/deep-tow investigation of an active oceanic propagating rift system, Galápagos 95.5 W, *J. Geophys. Res.*, 91(3), 3369–3393.
- Hey, R. N., J. M. Sinton, and F. K. Duennebieer (1989), Propagating rifts and spreading centers, in *The Geology of North America*, vol. N, *The Eastern Pacific Ocean and Hawaii*, edited by E. L. Winterer, pp. 161–176, Geol. Soc. of Am., Boulder, Colo.
- Humphris, S. E., G. Thompson, J.-G. Schilling, and R. H. Kingsley (1985), Petrological and geochemical variations along the Mid-Atlantic Ridge between 46°S and 32°S: Influence of the Tristan da Cunha mantle plume, *Geochim. Cosmochim. Acta*, 49(6), 1445–1464.
- Ito, G., and J. Lin (1995a), Oceanic spreading center-hotspot interactions: Constraints from along-isochron bathymetric and gravity anomalies, *Geology*, 23, 657–660.
- Ito, G., and J. Lin (1995b), Mantle temperature anomalies along the present and paleoaxes of the Galápagos spreading center as inferred from gravity analyses, *J. Geophys. Res.*, 100, 3733–3745.
- Ito, G., Y. Shen, G. Hirth, and C. J. Wolfe (1999), Mantle flow, melting, and dehydration of the Iceland mantle plume, *Earth Planet. Sci. Lett.*, 165, 81–96.
- Ito, G., J. Lin, and D. Graham (2003), Observational and theoretical studies of the dynamics of mantle plume–mid-ocean ridge interaction, *Rev. Geophys.*, 41(4), 1017, doi:10.1029/2002RG000117.
- Katz, R. F., M. Spiegelman, and S. M. Carbotte (2004), Ridge migration, asthenospheric flow and the origin of magmatic segmentation in the global mid-ocean ridge system, *Geophys. Res. Lett.*, 31, L15605, doi:10.1029/2004GL020388.
- Klein, E. M., and C. H. Langmuir (1989), Local versus global variations in ocean ridge basalt composition: A reply, *J. Geophys. Res.*, 94, 4241–4252.
- Kong, L. S. L., R. S. Detrick, P. J. Fox, L. A. Meyer, and W. B. Ryan (1989), The morphology and tectonics of the MARK area from Sea Beam and SEA MARC I observations (Mid-Atlantic Ridge 23°N), *Mar. Geophys. Res.*, 10(1–2), 59–90.
- Lin, J., G. M. Purdy, H. Schouten, J. C. Sempere, and C. Zervas (1990), Evidence from gravity data for focused magmatic accretion along the Mid-Atlantic Ridge, *Nature*, 344, 627–632.
- Macdonald, K. C. (1986), The crest of the Mid-Atlantic Ridge: Models for crustal generation processes and tectonics, in *The Western North Atlantic Region*, edited by P. R. Vogt and B. E. Tucholke, pp. 51–68, Geol. Soc. of Am., Boulder, Colo.
- Macdonald, K. C., P. J. Fox, L. J. Perram, M. F. Eisen, R. H. Haymon, S. P. Miller, S. M. Carbotte, M.-H. Cormier, and A. N. Shor (1988), A new view of the mid-ocean ridge from the behaviour of ridge-axis discontinuities, *Nature*, 335, 217–225.
- Magde, L. S., and D. W. Sparks (1997), Three-dimensional mantle upwelling, melt generation, and melt migration beneath segments of slow spreading ridges, *J. Geophys. Res.*, 102(B9), 20,571–20,583.

- Magde, L. S., D. W. Sparks, and R. S. Detrick (1997), The relationship between buoyant mantle flow, melt migration, and gravity bull's eyes at the Mid-Atlantic Ridge between 33°N and 35°N, *Earth Planet. Sci. Lett.*, *148*(1–2), 59–67.
- Magde, L. S., A. H. Barclay, D. R. Toomey, R. S. Detrick, and J. A. Collins (2000), Crustal magma plumbing within a segment of the Mid-Atlantic Ridge, 35°N, *Earth Planet. Sci. Lett.*, *175*(1–2), 55–67.
- Mahoney, J. J., D. W. Graham, D. M. Christie, K. T. M. Johnson, L. S. Hall, and D. L. Vonderhaar (2002), Between a hot spot and a cold spot: Isotopic variation in the Southeast Indian Ridge asthenosphere, 86°E–118°E, *J. Petrol.*, *43*, 1155–1176.
- Mutter, C. Z. (1995), Seismic and hydrosweep study of the western Costa Rica Rift, *Eos Trans. AGU*, *76*(46), Fall Meet. Suppl., F595.
- Parmentier, E. M., and J. Phipps Morgan (1990), Spreading rate dependence of three-dimensional oceanic spreading center structure, *Nature*, *348*, 325–328.
- Perram, L. J., and K. C. Macdonald (1994), An overlapping propagating spreading center at 87°30'W on the Galápagos spreading center, *Earth Planet. Sci. Lett.*, *121*(1–2), 195–212.
- Phipps Morgan, J., and E. M. Parmentier (1984), Lithospheric stress near a ridge-transform intersection, *Geophys. Res. Lett.*, *11*, 113–116.
- Phipps Morgan, J., and E. M. Parmentier (1995), Crenulated seafloor: Evidence for spreading-rate dependent structure of mantle upwelling and melting beneath a mid-oceanic spreading center, *Earth Planet. Sci. Lett.*, *129*, 73–84.
- Phipps Morgan, J., D. W. Caress, J. A. Orcutt, J. Minister, and M. C. Kleinrock (1988), Sea Beam magnetics, and gravity data from the 95.5 degrees W propagating rift: Results from the Tortuga expedition (abstract), *Eos Trans. AGU*, *69*(44), Fall Meet. Suppl., 1430.
- Purdy, G. M., J. C. Sempere, H. Schouten, D. L. Dubois, and R. Goldsmith (1990), Bathymetry of the Mid-Atlantic Ridge, 24–31°N: A map series, *Mar. Geophys. Res.*, *12*(4), 247–252.
- Scheirer, D. S., and K. C. Macdonald (1993), Variation in cross-sectional area of the axial ridge along the East Pacific Rise: Evidence for the magmatic budget of a fast spreading center, *J. Geophys. Res.*, *98*, 7871–7885.
- Scheirer, D. S., E. T. Baker, and K. T. M. Johnson (1998), Detection of hydrothermal plumes along the Southeast Indian Ridge near the Amsterdam-St. Paul Plateau, *Geophys. Res. Lett.*, *25*(1), 97–100.
- Scheirer, D., D. Forsyth, J. Conder, M. Eberle, S. Hung, K. Johnson, and D. Graham (2000), Anomalous seafloor spreading of the Southeast Indian Ridge near the Amsterdam-St. Paul Plateau, *J. Geophys. Res.*, *105*, 8243–8262.
- Schilling, J.-G., R. H. Kingsley, and J. D. Devine (1982), Galápagos hot spot-spreading center system I. Spatial petrological and geochemical variations (83°W–101°W), *J. Geophys. Res.*, *87*, 5593–5610.
- Schilling, J.-G., M. Zajac, R. Evans, T. Johnston, W. White, J. O. Devine, and R. Kingsley (1983), Petrologic and geochemical variations along the Mid-Atlantic Ridge from 29°N to 73°N, *Am. J. Sci.*, *283*, 510–586.
- Schilling, J., D. Fontignie, J. Blichert-Toft, R. Kingsley, and U. Tomza (2003), Pb-Hf-Nd-Sr isotope variations along the Galápagos Spreading Center (101°–83°W): Constraints on the dispersal of the Galápagos mantle plume, *Geochem. Geophys. Geosyst.*, *4*(10), 8512, doi:10.1029/2002GC000495.
- Schouten, H., H. J. B. Dick, and K. D. Klitgord (1987), Migration of mid-ocean-ridge volcanic segments, *Nature*, *326*, 835–839.
- Sempéré, J.-C., G. M. Purdy, and H. Schouten (1990), Segmentation of the Mid-Atlantic Ridge between 24°N and 30°40'N, *Nature*, *344*, 427–431.
- Sempéré, J.-C., J. R. Cochran, and SEIR Scientific Team (1997), The Southeast Indian Ridge between 88°E and 118°E: Variations in crustal accretion at constant spreading rate, *J. Geophys. Res.*, *102*(B7), 15,489–15,506.
- Singh, S., et al. (2005), Discovery of axial magma chamber reflections beneath the Lucky Strike hydrothermal vents and volcano and its relationship with median valley faults, *Eos Trans. AGU*, *86*(52), Fall Meet. Suppl., Abstract OS22A-04.
- Sinton, J., R. Detrick, J. P. Canales, G. Ito, and M. Behn (2003), Morphology and segmentation of the western Galápagos Spreading Center, 90.5°–98°W: Plume-ridge interaction at an intermediate spreading ridge, *Geochem. Geophys. Geosyst.*, *4*(12), 8515, doi:10.1029/2003GC000609.
- Sloan, H., and P. Patriat (1992), Kinematics of the North American-African plate boundary between 28° and 29°N during the last 10 Ma: Evolution of the axial geometry, spreading rate and direction, *Earth Planet. Sci. Lett.*, *113*, 323–341.
- Small, C., and L. V. Danyushevsky (2003), Plate-kinematic explanation for mid-oceanic-ridge depth discontinuities, *Geology*, *31*(5), 399–402.
- Smith, D. K., and J. R. Cann (1993), Building the crust at the Mid-Atlantic Ridge, *Nature*, *365*, 707–715.
- Smith, D. K., M. Tolstoy, C. G. Fox, D. R. Bohnenstiehl, H. Matsumoto, and M. J. Fowler (2002), Hydroacoustic monitoring of seismicity at the slow-spreading Mid-Atlantic Ridge, *Geophys. Res. Lett.*, *29*(11), 1518, doi:10.1029/2001GL013912.
- Sparks, D. W., and E. M. Parmentier (1993), The structure of three-dimensional convection beneath oceanic spreading centres, *Geophys. J. Int.*, *112*, 81–91.
- Stein, S., H. J. Melosh, and J. B. Minster (1977), Ridge migration and asymmetric sea-floor spreading, *Earth Planet. Sci. Lett.*, *36*, 51–62.
- Thibaud, R., P. Gente, and M. Maia (1998), A systematic analysis of the Mid-Atlantic Ridge morphology and gravity between 15°N and 40°N: Constraints of the thermal structure, *J. Geophys. Res.*, *103*, 24,223–24,243.
- Tolstoy, M., A. J. Harding, and J. A. Orcutt (1993), Crustal thickness on the Mid-Atlantic Ridge: Bull's-eye gravity anomalies and focused accretion, *Science*, *262*, 726–729.
- Tucholke, B. E., J. Lin, M. C. Kleinrock, M. A. Tivey, T. B. Reed, J. Goff, and G. E. Jaroslow (1997), Segmentation and crustal structure of the western Mid-Atlantic Ridge flank, 25°25'–27°10'N and 0–29 m. y., *J. Geophys. Res.*, *102*(B5), 10,203–10,224.
- Wang, X., and J. R. Cochran (1993), Gravity anomalies, isostasy and mantle flow at the East Pacific Rise crest, *J. Geophys. Res.*, *98*, 19,505–19,531.
- Weiland, C. M., K. C. Macdonald, and N. R. Grindlay (1996), Ridge segmentation and the magnetic structure of the Southern Mid-Atlantic Ridge 26°S and 31°–35°S: Implications for magmatic processes at slow spreading centers, *J. Geophys. Res.*, *101*(B4), 8055–8074.
- White, W. M., A. R. McBirney, and R. A. Duncan (1993), Petrology and geochemistry of the Galápagos Islands: Portrait of a pathological mantle plume, *J. Geophys. Res.*, *98*(B11), 19,533–19,563.
- Wilson, D. S. (1992), Focused mantle upwelling beneath mid-ocean ridges: Evidence from seamount formation and isostatic compensation of topography, *Earth Planet. Sci. Lett.*, *113*, 41–55.